

DRAFT VERSION JANUARY 10, 2022
Typeset using L^AT_EX **manuscript** style in AASTeX62

THE INTERFACE BETWEEN THE OUTER HELIOSPHERE AND THE INNER LISM: MORPHOLOGY OF THE LOCAL INTERSTELLAR CLOUD, ITS HYDROGEN HOLE, STROMGREN SHELLS, AND ⁶⁰Fe ACCRETION*

JEFFREY L. LINSKY,¹ SETH REDFIELD,² AND DENNIS TILIPMAN³

¹*JILA, University of Colorado and NIST, Boulder, CO 80309-0440, USA*

²*Astronomy Department and Van Vleck Observatory, Wesleyan University, Middletown, CT 06459-0123, USA*

³*Astrophysics and Planetary Sciences Department and JILA, University of Colorado, Boulder, CO 80309-0440*

ABSTRACT

We describe the interface between the outer heliosphere and the local interstellar medium (LISM) surrounding the Sun. The components of the inner LISM are the four partially ionized clouds [the Local Interstellar Cloud (LIC), G cloud, Blue cloud, and Aql cloud] that are in contact with the outer heliosphere, and ionized gas produced by EUV radiation primarily from ϵ CMa. We construct the three-dimensional shape of the LIC based on interstellar line absorption along 62 sightlines and show that in the direction of ϵ CMa, β CMa, and Sirius B the neutral hydrogen column density from the center of the LIC is a minimum. We call this region the “hydrogen hole”. In this direction, the presence of Blue cloud absorption and the absence of LIC absorption can be simply explained by the Blue cloud lying just outside of the heliosphere. We propose that the outer edge of the Blue cloud is a Strömgren shell driven toward the heliosphere

Corresponding author: Jeffrey L. Linsky
jlinsky@jila.colorado.edu

* Based on observations made with the NASA/ESA Hubble Space Telescope obtained from the Data Archive at the Space Telescope Science Institute, which is operated by the Association of Universities for Research in Astronomy, Inc., under NASA contract NAS AR-09525.01A. These observations are associated with programs #12475, 12596.

by high pressures in the H II region. We find that the vectors of neutral and ionized helium flowing through the heliosphere are inconsistent with the LIC flow vector, and that the nearby intercloud gas is consistent with ionization by ϵ CMa and other stellar sources without requiring additional sources of ionization or million degree plasma. In the upwind direction, the heliosphere is passing through an environment of several LISM clouds, which may explain the recent influx of interstellar grains containing ^{60}Fe from supernova ejecta measured in Antarctica snow.

Keywords: ISM: atoms — ISM: clouds — ISM: structure — line: profiles — ultraviolet: ISM — ultraviolet: stars

1. INTRODUCTION

1.1. *Properties of partially ionized warm clouds in the local interstellar medium*

The Sun is surrounded by patchy network of warm (5,000–10,000 K) partially ionized gas clouds extending out to a distance of about 15 pc in the local interstellar medium (LISM). We have learned about the properties of these gas clouds from high-resolution spectra of absorption lines produced by interstellar gas along lines of sight to nearby stars and from satellite measurements of interstellar gas flowing through the heliosphere. [Crutcher \(1982\)](#) first reported that the radial velocities of interstellar absorption lines in the spectra of nearby stars are consistent with interstellar gas flowing toward the Sun from the direction of the Scorpio-Centaurus Association. Later investigations (e.g., [Lallement & Bertin 1992](#); [Frisch, Grodnicki, & Welty 2002](#)) found that the local interstellar gas flow has a number of velocity components with slightly different flow directions and speeds.

[Redfield & Linsky \(2008\)](#) subsequently identified 15 different velocity components of warm interstellar gas located within 15 pc of the Sun by analyzing interstellar absorption lines in *HST* spectra of 157 nearby stars. The measured radial velocities along the lines of sight to stars distributed within large solid angles allowed [Redfield & Linsky \(2008\)](#) to determine velocity vectors for each of the 15 clouds. Using these velocity vectors, [Malamut et al. \(2014\)](#) predicted accurate radial velocities for the interstellar gas along the lines of sight to all 34 stars observed in their new data set. This success

in predicting accurate radial velocities for these new sight lines demonstrated that these cloud vectors have accurate predictive power. Figure 1 shows the angular extent in Galactic coordinates of the four closest interstellar gas clouds named LIC, G, Blue, and Aql. The Local Interstellar Cloud (LIC) is so-named because its angular extent covers nearly half of the sky, implying that the Sun is located just inside of the LIC or possibly immediately outside. The decision as to which option is more likely valid requires a second data type — measurements of interstellar gas flowing through the heliosphere.

Table 1 compares the properties of the interstellar gas flowing through the heliosphere with the parameters of gas located in the four nearest interstellar clouds. The properties listed are the flow speeds (v_{LISM}) relative to the Sun, temperatures (T) inferred from the interstellar line widths, and the ecliptic longitude (λ) and latitude (β) of the flow. In the table, we list parameters for neutral and ionized helium gas flowing through the heliosphere from the LISM as measured by four spacecraft: the *Extreme Ultraviolet Explorer (EUVE)*, *Interstellar Boundary Explorer (IBEX)*, *Ulysses*, and the *Solar Terrestrial Relations Observatory (STEREO)*. *EUVE* measured the resonant scattering of solar EUV photons by inflowing neutral helium atoms. *IBEX* measured the direction of neutral helium atoms that flow through the heliosphere without direction changing collisions. The resulting parameters obtained from four analyses of *IBEX* data listed in the table are in excellent agreement, indicating that the inflow speed of LISM gas relative to the Sun’s motion though the LISM is about $v_{\text{LISM}}=26 \text{ km s}^{-1}$ and the inflow direction is given by ecliptic longitude $\lambda = 75.5^\circ$ and ecliptic latitude of $\beta = -5.2^\circ$. The most recent *IBEX* measurement of inflowing helium (Swaczyna et al. 2018) refers to the primary component, which is separated from the “warm breeze” secondary component.

The inflow direction of neutral helium observed by the *Ulysses* spacecraft and He^+ pick-up ions (PUI) measured with *STEREO* spacecraft data also agree with $\lambda = 75.5^\circ$. Helium pick-up ions are previously neutral helium atoms that were ionized by EUV photons or charge-exchange processes in the heliosphere, then picked-up by the magnetic solar wind and gravitationally focused into a cone in the downwind direction. Taut et al. (2018) have investigated possible systematic errors in the analysis of the *STEREO* He^+ pick-up ion data, but they found no significant change in λ compared to the earlier results (Möbius et al. 2015b), except for a more realistic assessment of the errors.

Since the analysis of *IBEX* data of neutral helium results in a tight coupling between v_{LISM} , λ , and β (McComas et al. 2015; Möbius et al. 2015a,b), independent measurements of λ from *Ulysses* and *STEREO* are essential in pinning down accurate values for v_{ISM} and β . There have been a number of studies concerning whether the inflow vector obtained from *IBEX* observations of neutral helium is affected by interstellar magnetic fields or by confusion with a second component of the inflowing helium, called the “Warm Breeze” (Kubiak et al. 2014), but these possible effects appear to be very small (Kubiak et al. 2016).

Included in Table 1 are the properties of the neutral hydrogen gas located in the nearby partially ionized LISM clouds. Redfield & Linsky (2008) obtained these properties from their analysis of interstellar absorption lines in *HST* spectra of nearby stars. Also included in the table is a reanalysis of the flow vector through the LIC including 25% more sightlines than were not available at the time of the 2008 paper. The addition of these new sightlines produced only a slight change in the LIC flow parameters. The LIC cloud provides the closest match to the inflow parameters provided by *IBEX*, *Ulysses*, and *STEREO*, but the match is not perfect. We will discuss this agreement or disagreement in Section 6.

Slavin & Frisch (2008) computed a model for the LIC with neutral hydrogen number density $n_{\text{HI}} = 0.19\text{--}0.20 \text{ cm}^{-3}$, electron density $n_e = 0.007 \pm 0.01 \text{ cm}^{-3}$ and temperature $T = 6300 \text{ K}$. Redfield & Linsky (2008) found that the temperature of gas in the LIC is $7500 \pm 1300 \text{ K}$, that the temperatures of the other clouds lie in the range $5300\text{--}9900 \text{ K}$, and that their neutral hydrogen column densities lie in the range $\log N_{\text{HI}} = 17.2\text{--}18.8$. The values of n_{HI} and n_e in the other clouds are unknown, although the clouds are likely partially ionized like the LIC.

The absence of interstellar absorption at the predicted LIC velocity in the direction of the Sun’s motion implies that the Sun will leave the LIC in less than 3000 years (Redfield & Linsky 2008). Frisch, et al. (2013) and Frisch et al. (2015) proposed that the inflow direction has changed over the last 40 years, suggesting that the heliosphere’s environment is changing in our lifetime. Lallement & Bertaux (2014), however, argued against changes in the neutral helium inflow direction based on a reanalysis of the *IBEX* data including dead-time counting effects and the ecliptic longitude

directions of pick-up ions measured by *STEREO*. Their conclusion was supported by the absence of any measurable change over a 20-year time span in the interstellar flow vector of neutral hydrogen measured by the Solar Wind ANisotropies (SWAN) experiment on *SOHO* (Koutroumpa, et al. 2017).

1.2. *What are the properties of the intercloud gas?*

The theoretical models of the interstellar medium proposed by Field, Goldsmith, & Habing (1969), McKee & Ostriker (1977), and Wolfire et al. (1995) describe the interstellar gas as consisting of three components: cold ($T \leq 50$ K) neutral and molecular gas, warm neutral or partially ionized gas, and million-degree low-density fully ionized plasma. These classical models assume that the three components are each in thermal equilibrium and coexist in pressure equilibrium, but steady state equilibrium is highly unlikely in the low density dynamic interstellar medium where the time scales for ionization and recombination are on the order of 10^7 years (Chassefiere et al. 1986). The warm partially ionized gas clouds within a few parsecs of the Sun have properties roughly consistent with the warm component predicted by the classical models, and dense cold molecular clouds are observed typically by CO and H I 21-cm emission. The nearest cold gas with a temperature of 15–30 K is the Leo cloud located at a distance between 11.3 and 24.3 pc from the Sun (Peek et al. 2011). However, numerical simulations by Berghöfer & Breitschwerdt (2002), which include supernova explosions and realistic thermal and dynamic processes, predict a very wide range of densities and temperatures in the ISM but no pressure equilibrium and no identifiable thermal phases.

The Sun is located in a low-density region called the Local Cavity that extends more than 80 pc in all directions (Frisch, Redfield, & Slavin 2011). Inside of the Local Cavity are at least 15 partially ionized warm clouds (Redfield & Linsky 2008) and intercluster gas that was originally assumed to be hot (roughly 10^6 K), fully ionized, and low density (roughly 0.005 cm^{-3}). This Local Hot Bubble model was supported by the predictions of the classical models and observations of diffuse soft X-ray emission detected by rocket experiments and the *ROSAT* satellite. However, the presence of hot gas in the Local Cavity is now challenged on the basis of the following observational problems presented by Welsh & Shelton (2009):

Solar wind charge exchange (SWCX) emission: The unexpected detection of X-ray emission from Comet Hyakutake (Lisse et al. 1996) led to the recognition that charge exchange reactions between solar wind ions and neutral gas in the heliosphere can produce X-ray emission (Cravens 1997) that is similar to the emission produced by a million degree plasma. This result led to two different scenarios: (1) that roughly half of the observed diffuse X-ray emission in the Galactic plane is produced by SWCX reactions inside the heliosphere with the other half produced by hot intercloud plasma (Robertson & Cravens 2003; Galeazzi et al. 2014), or (2) essentially all of the 0.75 keV emission in the Galactic plane is SWCX emission and there is no need for emission from a hot plasma except near the Galactic poles (Snowden et al. 1994; Cox 1998; Koutroumpa, et al. 2009; Koutroumpa 2012).

O VI absorption: If hot gas were present in the Local Cavity, then interstellar absorption in the far-ultraviolet lines of O VI would indicate that intermediate temperature ($T \approx 300,000$ K) gas is present where the hot gas comes in contact with cooler gas at the edges of the partially ionized warm gas clouds. O VI absorption lines are detected in the circumstellar environment of hot stars and at high Galactic latitudes where there is hot gas in contact with the Galactic halo, but O VI absorption is not detected in lines of sight towards stars within 58 pc of the Sun (Barstow et al. 2010). The intercloud gas must, therefore, be cooler than 300,000 K yet still be mostly ionized so as to not show neutral hydrogen absorption.

Pressure imbalance: If the diffuse X-ray emission were produced by hot plasma, then the inferred emission measure predicts a gas pressure $P/k = 10,000\text{--}15,000 \text{ cm}^{-3}\text{K}$ (Snowden et al. 2014b) that is much larger than the gas pressure in the warm partially ionized clouds like the LIC where $P/k \approx 2500 \text{ cm}^{-3}\text{K}$ (Redfield & Linsky 2008). While additional pressure terms (e.g., magnetic fields, cosmic rays, and ram pressure) may be important, the very large pressure difference argues against the presence of hot plasma at least in the Galactic plane.

Upper limits on EUV line emission: Upper limits for diffuse high-temperature emission obtained by the *EURD* (Espectrógrafo Ultra-violeta extremo para la Radiación Difusa) satellite

([Edelstein et al. 2001](#)) exclude significant emission from both 10^6 K and intermediate temperature (10^5 K) gas in the Local Cavity. Upper limits obtained with the *Cosmic Hot Interstellar Plasma Spectrometer (CHIPS)* satellite by [Hurwitz, Sasseen, & Sirk \(2005\)](#) for diffuse emission of Fe lines, in particular the Fe IX 171.1 Å line, are also inconsistent with the predicted emission from putative 10^6 K thermal plasma in the Local Cavity.

Given these strong arguments against the presence of hot gas in the Local Cavity except towards the Galactic poles, the gas located between the warm partially ionized clouds (intercloud gas) and elsewhere within 80 pc of the Sun must be ionized but not necessarily hot in order to be not detected as neutral gas. Upper limits on the non-SWCX X-ray emission requires that the intercluster gas must be much cooler than 10^6 K or have a very low emission measure as indicated by X-ray shadowing experiments (e.g., [Peek et al. 2011](#)) and by extreme ultraviolet spectroscopy ([Hurwitz, Sasseen, & Sirk 2005](#)).

Various authors have proposed different solutions to the intercloud gas problem by identifying different sources of past and present ionization. [Lyu & Bruhweiler \(1996\)](#) and [Breitschwerdt & Schmutzler \(1999\)](#) proposed that the intercloud gas is a recombining remnant of a past ionization event such as a supernova shock wave. In this non-equilibrium plasma, the degree of ionization can be far higher than the electron temperature of the gas. This model is supported by the presence of young massive stars in the nearby Scapius-Centaurus OB Association and the likely presence of a previous group of massive stars that produced many supernova explosions with the last supernova perhaps as recent as 0.5 Myr. [Welsh & Shelton \(2009\)](#) proposed a “Hot-Top model” in which there is no hot gas except near the Galactic poles, but elsewhere the intercloud gas is highly ionized with an electron temperature of about 20,000 K in rough pressure equilibrium with the partially ionized warm clouds. An important source of ionization is the EUV radiation from ϵ CMa, the brightest EUV source detected by the *Extreme Ultraviolet Explorer (EUVE)* satellite and other hot stellar and white dwarf sources ([Vallerga & Welsh 1995](#); [Vallerga 1998](#)). Among the nearby sources of EUV emission is Sirius B, located only 2.6 pc from the Sun.

Strömgren (1939) showed that the EUV emission of hot stars photoionizes the surrounding gas producing an HII region extending out to a distance that defines a classical Strömgren sphere. Our model for the intercloud gas near the Sun is a Strömgren sphere-like H II region photoionized primarily by ϵ CMa rather than a recombining plasma, because the ionization state of the gas seen towards ϵ CMa is modest (mostly singly-ionized atoms) and the EUV radiation field is very strong.

1.3. *Outline of this paper*

In this paper, we describe the properties of the partially ionized warm gas clouds in the immediate neighborhood (within 4 pc) of the Sun and the intercloud gas present between these clouds. In a subsequent paper, we will extend this analysis further into the LISM. In Sections 2 and 3, we measure the size and shape of the LIC from 62 column densities of D I, Fe II, and Mg II. Section 4 describes the properties of Strömgren spheres of ionized gas surrounding nearby hot stars and white dwarfs. In Section 5, we identify the hydrogen hole in the LIC, which is photoionized by EUV radiation primarily from ϵ CMa, and propose that the Blue cloud in the direction of the hydrogen hole is a Strömgren shell. In Section 6 we consider whether the flow vector measured by *IBEX* and other satellites is inconsistent with the LIC flow vector measured from interstellar absorption lines, and, if so, what information can be gleaned from this inconsistency. In Section 7, we identify the gas clouds and intercloud components in the sightlines to nearby stars, In Section 8 we propose that the recent measurement in Antarctic snow of interstellar grains containing ^{60}Fe from a supernova could be explained by the inflow of dust grains from warm clouds in contact with the heliosphere either at a continuous low level rate or during an unusual event. Finally, we list our conclusions and needed future work.

2. DATA ANALYSIS

2.1. *Estimating distances to the edge of the LIC*

The procedure for estimating distances to the edge of the LIC is conceptually straightforward. We assume that the LIC surrounds the heliosphere in most directions and has constant neutral hydrogen density $n(\text{H I})$. Therefore, the neutral hydrogen column density $N(\text{H I})$ divided by $n(\text{H I})$ gives the

path length of the absorbing medium, which in this case is simply the distance to the edge of the LIC along this line of sight (LOS). A fairly robust measurement of $n(\text{H I})$ exists for the immediate vicinity of the Sun, derived from (a) Lyman- α backscatter estimates (Quemerais et al. 1994), (b) *in situ* neutral helium measurements (Gloeckler et al. 2004), and (c) He I/H I measurements from extreme-UV observations of local white dwarfs (Dupuis et al. 1995). These diverse measurements indicate that $n(\text{H I}) \approx 0.2 \text{ cm}^{-3}$ in the immediate vicinity of the Sun. This density is slightly higher than the lower limit of $n(\text{H I})$ derived from dividing $N(\text{H I})$ by the distance to the nearest observed stars, which has a maximum value of $\langle n(\text{H I}) \rangle \sim 0.1 \text{ cm}^{-3}$. This difference between $n(\text{H I})$ and $\langle n(\text{H I}) \rangle$ indicates that either the filling factor of warm gas inside the LIC and presumably other clouds is less than unity or that the portion of the LIC very close to the Sun has a higher density than elsewhere in the LIC (Redfield & Linsky 2008). In addition, several sight lines to nearby stars (e.g., 61 Cyg, α CMi, and α Aql) limit the average value of $\langle n(\text{H I}) \rangle$ to $\leq 0.2 \text{ cm}^{-3}$.

Hydrogen column densities, however, are difficult to measure towards nearby stars. The strongest transition (e.g., Lyman- α) is saturated, contaminated by airglow emission, and complicated by heliospheric and astrospheric absorption (Wood et al. 2005). We, therefore, estimate $N(\text{H I})$ from other available atoms and ions in the following priority: D I, Fe II, and Mg II. Deuterium is an excellent tracer of hydrogen due to its tight abundance ratio within the Local Bubble, $\text{D}/\text{H} = 15.6 \pm 0.4 \times 10^{-6}$ (Linsky et al. 2006). Both Fe II and Mg II are the dominant ionization stages for these elements, and despite significant depletion onto dust grains, they have relatively tight and narrow correlations with hydrogen. Also, these three ions are commonly observed. Of the 79 sight lines assigned to the LIC on the basis of their radial velocities being consistent with the LIC velocity vector (Redfield & Linsky 2008), 64 (81%) have observations in one or more of these ions. The remaining LIC sight lines were detected in Ca II alone. Most measurements were taken from compilations of observations of these ions from Redfield & Linsky (2004a) for D I and Redfield & Linsky (2002) and Malamut et al. (2014) for Fe II and Mg II.

We use LIC sight lines with measurements of D I, Fe II, and Mg II to empirically determine the appropriate conversion to hydrogen column densities. Redfield & Linsky (2008) calculated the

depletion of Fe II and Mg II inside the LIC based on 12 sight lines with both D I and Fe II, and 21 sight lines that have both D I and Mg II observations. The weighted mean value of Fe II/H I, where the hydrogen column density is calculated from D I and the well-determined D/H ratio given above, is $\langle \text{Fe II/H I} \rangle = 2.14^{+0.61}_{-0.48} \times 10^{-6}$, and for magnesium, $\langle \text{Mg II/H I} \rangle = 3.6^{+2.8}_{-1.6} \times 10^{-6}$. The errors include the error in the D/H ratio, as well as the standard deviation in the distribution of measurements, which would include any depletion or ionization variations within the LIC.

Figure 2 shows a comparison of the estimated H I column densities based on observations of the three ions (D I, Mg II, and Fe II). Typical errors in the log H I column density estimate based on D I are only ~ 0.09 , while for Mg II and Fe II they are 0.35 and 0.27, respectively. Note the tight correlation and small errors associated with D I. For all three comparison plots, $\sim 77\%$ of the data pairs predict consistent values for $N(\text{H I})$ pairs within 1σ . While there is a large dispersion in the comparison of $N(\text{H I})$ for Mg II and Fe II, they still seem to be relatively good proxies for the H I column density, provided there is a sensible estimate of the elemental depletion.

Other ions were investigated, but they suffer more seriously from ionization and depletion effects. For example, Ca II is not the dominant ionization stage of calcium in the LISM, but makes up only 1.6% of the gas phase calcium, whereas 98.4% is expected to be in Ca III (Slavin & Frisch 2008). For this reason, the Ca II/H I ratio varies much more significantly than the corresponding ratios for Mg II and Fe II, and does not provide a useful means of estimating the hydrogen column density.

The magnitudes of the errors in the abundance ratio to hydrogen (X/H) clearly show that deuterium measurements are most desirable, typically followed by Fe II, and then by Mg II. Both the Fe II and Mg II measurements are given for all LIC sight lines in Table 2. Along six lines of sight, both Fe II and Mg II were measured and are listed in the table. In all six cases, the two ions lead to $N(\text{H I})$ estimates that agree to within 3σ . The estimates of $N(\text{H I})$ used in the subsequent analysis are typically the ones with higher accuracy, which for these sight lines without D I data were obtained from Fe II in all cases. Of the 67 sight lines with observations of the LIC in one of these three ions, 34 (51%) have D I observations, 19 (28%) have Fe II but no D I, and 14 (21%) were observed in Mg II

alone. Table 2 identifies each sight line, and which ion was used in the H I calculation. We assume $n(\text{H I}) = 0.2 \text{ cm}^{-3}$ to calculate the distance from the Sun to the edge of the LIC.

Sight lines in which the relative error in the distance to the LIC edge $[\sigma(d_{\text{edge}})/d_{\text{edge}}]$ is of order unity (i.e., >0.9) were removed from the sample, as they do not provide any significant constraint on the distance to the LIC edge and result typically from large errors in the measured ion column density because of saturation or the difficulty in establishing the velocity component structure of blended profiles. Only 3 sight lines were removed ($\sim 4\%$ of the sample) for this reason. In addition, sight lines for which the distance to the LIC edge is estimated at more than 5 standard deviations from the median value were also removed. Again, it is possible that these are due to erroneously large column density measurements (in all cases they were larger than the median value) due to saturation or blending. Five measurements were thus removed ($\sim 7\%$ of the sample), with three of them observed in Fe II and two in Mg II (which had complimentary Fe II observations that could be used). No targets observed in D I were removed for these reasons. We note that three of these targets are roughly in the same part of the sky ($l=47^\circ\text{--}57^\circ$, $b=27^\circ\text{--}32^\circ$): 72 Her, 99 Her, and HD157466. They all have nearly saturated absorption lines, leading to the large column densities and high path length measurements with large errors. This part of the sky is near the upwind direction and is complicated by the presence of several LISM clouds (see Fig. 19 in Redfield & Linsky 2008). Also, other LIC absorbers in the vicinity (e.g., γ Ser, α Oph, δ Cyg, ι Oph) show relatively high column densities. Three of these sight lines were observed only in Ca II (α Oph, δ Cyg, ι Oph), but have among the highest values of $N(\text{H I})$ detected in the LISM (see Fig. 7 in Redfield & Linsky 2002). While γ Ser and α Lyr are both within 5σ of the mean LIC path length, both have observed values that are 2.7σ from the predicted value based on our morphological model. Clearly, something complex and interesting is occurring in this region of the sky.

A significant number of the D I measurements were made without full knowledge of the velocity component structure. If more than one absorbing cloud is present along the line of sight, this can lead to overestimated column densities if the profile is modeled as a single component. Due to the strong thermal broadening of D I (Redfield & Linsky 2004b), multiple velocity components are not

immediately obvious and thus require observations at high resolution of heavier ions such as Fe II or Mg II to infer a more accurate value of $N(\text{H I})$. Because the contributions of such possible systematic errors are not included in the D I column density estimate, we treat the estimates derived from these sight lines with caution. Of the 34 D I measurements, this effects 11 (32%) of them (τ Cet, δ Eri, EP Eri, HR1925, HR8, DX Leo, PW And, SAO136111, V471 Tau, HR1608, and Feige 24). Future short observations of Fe II or Mg II could easily resolve the component structure and greatly improve the accuracy of the D I analysis (e.g., [Malamut et al. 2014](#)).

3. MORPHOLOGY OF THE LOCAL INTERSTELLAR CLOUD (LIC)

Motivated by a significant increase in the number of observations of the LISM, we present a revised analysis of the three-dimensional morphology of the interstellar material that directly surrounds our solar system, the Local Interstellar Cloud (LIC). We follow the same procedure outlined in [Redfield & Linsky \(2000\)](#), which involves fitting a series of spherical harmonics to the estimated distances to the edge of the LIC given in Table 2. As in [Redfield & Linsky \(2000\)](#), we fit the data to 9 basis functions (e.g., $l = 0, 1, 2$). We assume a homogeneous and constant density cloud in order to estimate the distance to the edge of the LIC from our column density measurements. In Section 6 we will test the validity of these assumptions. With a large enough sample and corresponding high orders of spherical harmonics, any arbitrary closed surface can be characterized with this technique. The best fitting amplitude for each spherical harmonic basis function is determined using a least-squared minimization routine.

There are two significant changes in our analysis compared to [Redfield & Linsky \(2000\)](#). First is the quantity and quality of the input data. In order to have a sufficient number of data points, [Redfield & Linsky \(2000\)](#) used hydrogen column density measurements derived from observations using *HST*, *EUVE*, and ground-based Ca II. This resulted in a sample comprised of 32 measurements. In the current analysis, we limit ourselves to a homogenous sample of only the highest quality column density measurements, derived from *HST* spectra. Given the significant increase in LISM measurements (e.g., [Redfield & Linsky 2002, 2004a](#); [Malamut et al. 2014](#)), our current sample includes 62 measurements.

The second significant difference with the [Redfield & Linsky \(2000\)](#) analysis, is our improved knowledge of the hydrogen volume density in the LISM. [Redfield & Linsky \(2000\)](#) used a value of $n_{\text{HI}} = 0.1 \text{ cm}^{-3}$, based on limits toward the nearest stars. However, we now estimate the neutral hydrogen density to be closer to $n_{\text{HI}} = 0.2 \text{ cm}^{-3}$ ([Slavin & Frisch 2008](#)). Therefore, our estimates for the size of the LIC will be roughly a factor of two smaller than in [Redfield & Linsky \(2000\)](#) as distances are inversely proportional to the assumed neutral hydrogen number density.

The resulting parameters of the best fit spherical harmonics model is given in Table 3. Like the original model in [Redfield & Linsky \(2000\)](#), the dominant harmonic is the spherical $l = 0$ component indicating that to first-order the LIC can be characterized as a quasi-spherical closed volume. However, the contributions of the additional spherical harmonic orders lead to significant departures from a pure sphere. Contours of the best fit three-dimensional model are shown in Figures 3–5. The shape is much better constrained than in the [Redfield & Linsky \(2000\)](#) model, although the general geometry is not all that different. In particular, the observations continue to support the interesting conclusion that the Sun is located very near to the edge of the LIC, indicating that in as little as ≈ 3000 years, the Sun will pass out of the LIC and into a different interstellar environment.

The geometry of the LIC can also be visualized in Figure 6, where the shading indicates the distance to the edge of the LIC from the geometric center of the LIC (as given in Table 3). The reduced χ^2 is relatively high, indicating that there are significant departures from this relatively simple model. In particular, out of 62 total data points, 26 (42%) are within 1σ , 38 (61%) within 2σ , and 54 (87%) within 3σ . The most discrepant sight lines are toward η Ari (for which the model predicts a larger distance than the observations imply) and τ^6 Eri (for which the model predicts a much closer distance than the observations imply). Some of the discrepancies could be explained by misidentifications or blends of multiple components as singular LIC absorption features. However, it is likely that our simple assumptions of homogeneity and constant density are, unsurprisingly, not completely realistic. While, by and large, the structure is well characterized in this way, there are likely to be regions where there are significant departures in homogeneity or density that lead to discrepancies between the model and observations.

4. WHAT IS THE IONIZATION SOURCE FOR THE INTERCLOUD GAS NEAR THE SUN?

The brightest nonsolar source of extreme-UV radiation detected by the EUVE satellite was the B2 II star ϵ CMa ($d=124$ pc) with an intrinsic ionizing flux of about $2.7 \times 10^{46} \text{ s}^{-1}$ (Vallerga & Welsh 1995). This flux estimate includes a correction for absorption by a hydrogen column density, $N(\text{H I})=9 \times 10^{17} \text{ cm}^{-2}$, along the line of sight to the star. If the Gry et al. (1995) estimate of $N(\text{H I}) < 5 \times 10^{17} \text{ cm}^{-2}$ is more realistic, then the intrinsic ionizing flux from ϵ CMa will be larger. The next brightest EUV source is β CMa (B1 II-III; $d=151$ pc), followed by many hot white dwarfs located inside of the Local Bubble (Vallerga 1998). The total ionization rate of 33 hot white dwarfs measured by EUVE is $\sim 1.6 \times 10^{45} \text{ photons s}^{-1}$ (Welsh et al. 2013), which is more than a factor of 10 times smaller than the ionizing flux from α CMa.

In a classic paper, Strömgren (1939) showed that the EUV radiation ($\lambda < 912 \text{ Å}$) from a hot star completely ionizes hydrogen in its surrounding volume (called a Strömgren sphere) out to a distance now called the Strömgren radius where the build up of neutral hydrogen opacity absorbs the photoionizing radiation, producing a narrow partially ionized shell surrounded by neutral hydrogen gas. In this paper, Strömgren developed a simple model assuming that the hot star is located in a constant density environment in which flows are ignored and photoionization of hydrogen is balanced by recombination in a steady state. In this case, the radius of the classical Strömgren sphere is

$$R^3 = 3(dN_i/dt)/(4\pi\alpha n_i n_e), \quad (1)$$

where dN_i/dt is the number of ionizing photons per second and n_i and n_e are the number densities of ions and electrons inside of the Strömgren sphere, and α is the recombination factor (Harwit 1988). For relatively soft stellar radiation such as from ϵ CMa where most of the ionizing radiation is in the 504–912 Å band, hydrogen inside of the Strömgren sphere will be fully ionized and helium mostly neutral. When the radiation field is harder with significant radiation as wavelengths shortward of the 504 Å photoionization edge of He^0 or the 228 Å photo-ionization edge of He^+ , as is the case for very hot white dwarfs such as G191-B2B and HZ 43, then helium will be either singly or doubly ionized. Tat & Terzian (1999) estimated the sizes of Strömgren spheres around hot white dwarfs in the Local

Cavity using the classical Strömgren sphere model. This model has been extended to include dust opacity, clumpiness, diffuse radiative transfer, and dynamics (e.g., [Yorke 1986](#)). [McCullough \(2000\)](#) computed modified Strömgren sphere models for the case of a hot star embedded in a larger ionized cavity. Depending on the location of the hot star in the cavity, the H II region around the star is no longer a sphere. Rather, the H II region produced by the hot star is larger than for the classic case because the surrounding gas is not neutral and the two H II regions can merge. Since Sirius B resides inside of the H II region produced by ϵ CMa, we refer to the H II region near Sirius B as an “extended H II region”.

The electron density in the line of sight to ϵ CMa is unknown, but if it is about 0.01 cm^{-3} , then the radius of the star’s Strömgren sphere equals the distance to the star (130 pc). This is consistent with the conclusion by [Welsh et al. \(2013\)](#) that ϵ CMa is the primary source responsible for the ionization of the local ISM. They found that the volumetric filling factor of the classical Strömgren spheres of all 33 of the hottest white dwarfs (excluding Sirius B) in the Local Cavity is less than 6% and that none of these hot white dwarfs are close enough to the Sun to influence the local ionization.

We next consider whether Sirius B could be an important local ionization source given its short 2.6 pc distance from the heliosphere. Fitting the *HST* spectrum of Sirius B with a non-LTE model atmosphere, [Barstow et al. \(2005\)](#) obtained the stellar parameters $T_{\text{eff}} = 25,193 \text{ K}$, $\log g = 8.556$, and radius 0.0081 solar. Martin Barstow (private communication) kindly computed the flux shortward of 912 \AA for this model as $9.4 \times 10^{39} \text{ photons s}^{-1}$. The radius of a classical Strömgren sphere for this photon flux is 0.25 pc for an assumed $n_e = 0.1 \text{ cm}^{-3}$ ([Redfield & Falcon 2008](#)) or 1.14 pc for an assumed $n_e = 0.01 \text{ cm}^{-3}$. These calculations are for an isolated Strömgren sphere surrounded by neutral hydrogen, but Sirius B is embedded in the large H II region ionized by ϵ CMa, and the physical conditions of interstellar gas near Sirius and the Sun are controlled by stellar radiation in the 504–912 \AA region and by hot white dwarfs at shorter wavelengths.

Table 4 lists the stars within 16 pc of the Sun for which neutral hydrogen column densities through the nearby clouds have been measured by [Redfield & Linsky \(2008\)](#) and by [Malamut et al. \(2014\)](#). We list the distances through neutral hydrogen gas, $\Delta d(\text{neutral})$, along the lines of sight (LOS) through

the identified clouds, assuming that the neutral hydrogen density is the same as that measured for the LIC ($n_{HI} = 0.2 \text{ cm}^{-3}$) by [Slavin & Frisch \(2008\)](#). We presume that the remaining path length $\Delta d(\text{ionized})$ is filled by ionized gas, but we revisit this assumption when we discuss the G cloud sight line in Section 7.

We note that the thickness of the partially ionized outer shell of a Strömgren sphere is $\delta = (n_{HI}\sigma)^{-1}$, where $\sigma \approx 10^{-17} \text{ cm}^2$ ([Harwit 1988](#)) is the hydrogen-ionization cross section for EUV photons near 912 Å. Thus for $n(\text{H I}) \approx 0.2 \text{ cm}^{-3}$, the Stromgren shell thickness is $\delta \approx 0.2 \text{ pc}$. Filamentary warm clouds like the Mic Cloud could have roughly this thickness.

The incident EUV radiation from ϵ CMa should produce higher ionization inside H II regions and Strömgren shells. [Gry et al. \(1995\)](#) found interstellar absorption by Si III and C IV at the predicted LIC velocity in the sight line to ϵ CMa, although the C IV absorption could be in the stellar wind. [Dupin & Gry \(1998\)](#) also found C IV absorption at the LIC cloud velocity in the sight line to β CMa. Since both sight lines pass through Strömgren shells, there is strong evidence for higher ionization in these shells.

In Table 5, we compare the thicknesses of the LIC and Blue clouds seen in the directions of ϵ CMa and Sirius. The cloud thicknesses in these directions are consistent with their being Strömgren shells. It is likely that the outer edges of all clouds facing the EUV radiation from ϵ CMa are Strömgren shells.

5. THE HYDROGEN HOLE AND BLUE CLOUD HAVE A COMMON ORIGIN

Figure 6 shows the distance to the edge of the LIC from its geometric center computed from the measured values of $N(\text{H I})$ along the lines of sight to nearby stars. The region within Galactic longitude $225^\circ \leq l \leq 290^\circ$ and Galactic latitude $-60^\circ \leq b \leq +10^\circ$ shows very low H I column densities corresponding to a skin depth of $< 0.5 \text{ pc}$ from the geometric center of the LIC. We call this region the “hydrogen hole”. The Galactic coordinates of ϵ CMa, β CMa, and Sirius as seen from the center of the LIC all lie within this region. The location of the hydrogen hole is consistent with the coordinates of these three strong sources of ionizing radiation that apparently shape the morphology of the LIC in the ϵ CMa direction. [Welsh et al. \(1999\)](#) refer to the low hydrogen column density

along the lines of sight to ϵ CMa and β CMa as an interstellar tunnel or local chimney that extends beyond these stars to the Galactic halo.

Figure 7 shows the distance in pc from the geometric center of the LIC to its edge along the sightlines to the 10 brightest EUV sources observed by the *EUVE* spacecraft (Vallerga & Welsh 1995). The lines of sight to the brightest EUV source ϵ CMa and four of the five next brightest sources all have the shortest distances from the center of the LIC edge to its edge, which is consistent with EUV radiation sculpting the LIC by photoionizing neutral hydrogen.

We now consider what type of gas lies immediately outside of the heliosphere in the direction of the hydrogen hole. Three possibilities are (i) a very thin layer of partially ionized LIC cloud gas, (ii) partially ionized gas of another cloud, or (iii) fully ionized hydrogen gas (H II region). A test for the first two possibilities would be the detection of Lyman- α absorption in the hydrogen wall near the Sun where the inflowing neutral hydrogen atoms from a partially ionized cloud (LIC or another cloud) charge-exchange with the outflowing protons in the solar wind leading to a pile-up of heated, red shifted, neutral hydrogen atoms. The result would be Lyman- α heliospheric absorption that is red shifted relative to the inflowing neutral hydrogen. Table 6 summarizes the data for those stars located inside of or near the region of minimum $N(\text{H I})$ that have detected or nondetected solar hydrogen wall absorption. The data fall into three groups detailed in Sections 5.1 to 5.3.

5.1. Stars well inside of the hydrogen hole

The nine stars with lines of sight that traverse the hydrogen hole all show an absorption component at the predicted Blue cloud radial velocity and, except for ϵ CMa, no absorption component at the predicted LIC radial velocity. Three nearby stars, ζ Dor, HR 2225, and HR 2882, also do not show solar hydrogen wall absorption that would indicate the absence of neutral hydrogen in the interstellar gas immediately outside of the heliosphere. For the other six stars there are no high-resolution Lyman- α spectra needed to determine whether or not they show solar hydrogen absorption. However, all nine stars are located in the downwind direction of the LIC flow where it difficult to detect solar hydrogen wall absorption (Wood et al. 2005). Therefore, immediately outside of the heliosphere in the hydrogen hole direction there could be either Blue cloud or H II gas. We propose that Blue cloud

gas is in contact with the outer heliosphere along these lines of sight, and that ionized hydrogen gas is located outside of the Blue cloud where it receives unattenuated EUV radiation from ϵ CMa and Sirius.

In their study of the ϵ CMa line of sight with the Ech B and G160M gratings on *HST*/GHRS, Gry et al. (1995) found absorption at the predicted radial velocities of the LIC and Blue clouds (their components 1 and 2). The low value for the hydrogen column density for component 1, $\log N(\text{H I}) \approx 17.34$, implies that the line of sight passes through the edge of the LIC (see Figure 8), and the gas temperature $T = 7450$ K is similar to that found by Redfield & Linsky (2008) for the LIC. For the Blue cloud, the inferred neutral hydrogen column density is also very small, $\log N(\text{H I}) = 16.88$, and the cloud gas temperature is low, $T = 3600 \pm 1500$ K, similar to that found by Redfield & Linsky (2008). The electron density in the Blue cloud, $n_e = 0.46^{+0.40}_{-0.30} \text{ cm}^{-3}$, found by Gry et al. (1995) could be much larger than what they found for the LIC, $n_e = 0.09^{+0.23}_{-0.07} \text{ cm}^{-3}$. The high electron density of the Blue cloud, **if real**, could be explained either by a higher total density or less shielding from the EUV radiation of ϵ CMa compared to the LIC or both effects. In addition to interstellar absorption in low excitation lines, Gry et al. (1995) also found absorption features in the C IV lines at the predicted radial velocity of the LIC cloud. They could not rule out the possibility that the C IV absorption is stellar, perhaps from the star's wind, rather than interstellar. Further study is needed to determine whether the absorption indicates the presence of highly ionized gas surrounding the cooler material in the LIC and Blue clouds.

Interstellar absorption along the line of sight to β CMa has been studied by Dupin & Gry (1998) using UV spectra from *HST*/GHRS and by Jenkins et al. (2000) using UV spectra from the *IMAPS* instrument. In their paper, Jenkins et al. (2000) identified a velocity component that is at the predicted radial velocity of the Blue cloud. There is also absorption at the predicted radial velocity of the LIC, but Jenkins et al. (2000) argued that this absorption is not likely from the LIC on the basis of the unrealistically high ionization required to fit the observed absorption in many ions.

5.2. Stars near the edge of the hydrogen hole

Five stars are located near the edge of the hydrogen hole either just inside or outside. Four show LIC absorption and one (Sirius) also shows solar hydrogen wall absorption. At the outer edge of the hydrogen hole, therefore, LIC gas is in contact with the outer heliosphere. For the lines of sight that also show Blue cloud absorption, we place the Blue cloud just outside of the LIC.

5.3. *Stars outside of but near the hydrogen hole*

Outside of the hydrogen hole at Galactic longitudes greater than $l=280^\circ$, five of the six stars have solar hydrogen wall detections and all six have no detected absorption at radial velocities predicted by the LIC velocity vector. In these directions there must be neutral hydrogen gas flowing into the heliosphere to create the solar hydrogen wall, but this neutral gas has the velocity vector of the G or Aql cloud rather than the LIC.

5.4. *Comparison of the Blue cloud with the hydrogen hole*

Figure 8 shows the outer contours of the hydrogen hole and the locations of ϵ CMa, β CMa and some of the stars in Table 6 plotted in Galactic coordinates. Superimposed on the hydrogen hole is the boundary of the Blue cloud based on Figure 3 in Redfield & Linsky (2008) and the stars listed in Table 6. The similar morphologies of the hydrogen hole and the Blue cloud strongly imply their physical connection. The radial velocity of the Blue cloud in the direction of ϵ CMa is 12.97 km s^{-1} , which is blue shifted about 6 km s^{-1} relative to the predicted LIC velocity for this line of sight. We interpret the Blue cloud as a Strömgren shell that is driven towards the heliosphere by excess pressure in the external H II region. The Blue cloud's lower temperature and higher gas density than the LIC could result from compression of the Blue cloud gas leading to increased radiative cooling compared to the LIC.

We conclude from this analysis that in the hydrogen hole direction, lines of sight from the Sun first pass through the Blue cloud and then through ionized gas. Outside of the hydrogen hole at larger Galactic longitudes, the lines of sight from the Sun pass through the G or other clouds rather than the LIC. The stars lying at the edge of the hydrogen hole and ϵ CMa have lines of sight that first

encounter a small column density of LIC gas. The absence of LIC gas inside most of the hydrogen hole confirms that the heliosphere lies at the edge of or just beyond the LIC.

6. IS THE LIC FLOW VECTOR CONSISTENT WITH MEASUREMENTS OF INTERSTELLAR GAS FLOWING THROUGH THE HELIOSPHERE?

In Section 1, we called attention to the flow vector for neutral and singly ionized helium near the heliosphere inferred from observations with the *EUVE*, *IBEX*, *Ulysses*, and *STEREO* spacecraft. This vector, which we call the “inflow vector”, refers to gas just before entering the heliosphere where interactions with the Sun’s gravity, radiation pressure, and solar wind particles can alter the flow direction. The excellent agreement in speed, flow direction and temperature among these different measurement techniques by different instruments provides the benchmark for the flow vector of interstellar gas just outside of the heliosphere. The flow vector of neutral hydrogen in the LIC cloud, which we call the “LIC vector”, refers to gas located at one or a few parsecs from the heliosphere where possible influences from the Sun and the solar wind are negligible. Here we consider whether the inflow and LIC vectors are in agreement, or whether they differ due to some effect not yet taken into consideration. There are several possibilities:

The inflow and LIC vectors agree within measurement errors: The data in Table 1 shows that the gas temperatures of the two vectors are in agreement, but the inflow speed of the LIC gas is $2\text{--}3 \text{ km s}^{-1}$ too slow, the ecliptic longitude of the LIC flow is about 3° too high, and the ecliptic latitude about 2° too low. However, the difference in speed is only about 2.2σ and the difference in flow directions only 1σ . Given these small differences, one could argue that the inflow and LIC flow vectors agree, but new studies are needed to reduce measurement errors and provide insight into the magnitude of potential systematic errors.

The LIC flow may be inhomogeneous: The difference in flow speeds of the two vectors, if real, could test the kinematics of the LIC gas. There is no physical reason why the low density gas in the LIC should have homogeneous flow properties. In fact, the mean nonthermal broadening of interstellar absorption lines in the LIC, $\xi = 1.62 \pm 0.75 \text{ km s}^{-1}$ (Redfield & Linsky 2008),

is nearly as large as the difference in speed between the inflow and LIC vectors. Other nearby interstellar clouds have values of ξ as large as 3.6 km s^{-1} , about half of the cloud's sound speed. Gry & Jenkins (2014) have proposed that the multicloud scenario can be replaced by a single interstellar cloud with velocity gradients, but Redfield & Linsky (2015) have argued that the data are more accurately fit with multiple clouds each with its own velocity vector.

As a test for an inhomogeneous flow pattern in the LIC gas, we have selected LIC velocity components that meet the following criteria: (a) the uncertainty in the measured radial velocity is no more than three times the precision of the instrumental velocity scale (typically 1.5 km s^{-1}), and (b) that the distance from the Sun is no more than 4 pc. The latter criterion removes velocity components with large uncertainties in $N(\text{H I})$. Of the 62 LIC velocity components, 45 meet both criteria. Figure 9 shows the deviations in the measured radial velocities from those predicted by the LIC velocity vector. The velocity deviations appear to be random, except for an excess of blue points (positive radial velocities) near $l = 180^\circ$ and $b = -25^\circ$. It is interesting that this location is close to the tail of the LIC flow, $l = 187.0^\circ \pm 3.4^\circ$ and $b = -13.5^\circ \pm 3.3^\circ$ (Redfield & Linsky 2008). The reality of this region of velocity deviation and a physical explanation for the similar direction as the tail of the LIC flow requires additional data and investigation.

The LIC flow at its outer edge may differ from its mean value: Outside of the hydrogen hole, a thin region of LIC gas could be in contact with the ionized gas produced by radiation from ϵ CMa and Sirius. Contact with this ionized gas can alter the flow of the adjacent LIC gas by a pressure difference if the ionized gas has a higher or lower pressure than the LIC.

Could hydrogen and helium in the LIC have different flow vectors?: Since the inflow vector is measured from neutral and ionized helium and the LIC vector is measured from neutral hydrogen, we consider whether hydrogen and helium could have different inflow vectors. Lallement et al. (2005) compared the inflow direction of neutral helium with that of neutral hydrogen observed from the glow of backscattered solar Lyman- α photons that were observed

by the Solar Wind Anisotropies (SWAN) instrument on the *Solar and Heliospheric Observatory* (*SOHO*). The inflow directions of neutral helium and hydrogen differ by about 4° (see Table 1), which they explain as due to the inflowing hydrogen being a mixture of pristine interstellar hydrogen and hydrogen atoms resulting from charge exchange between solar wind electrons and interstellar protons. The properties of this hydrogen with mixed origins is very different from the pristine interstellar helium observed by *IBEX*, *Ulysses*, and *STEREO* and from the hydrogen observed at parsec distances by UV spectroscopic measurements. Thus the question of whether there is a difference between the flow vectors of hydrogen and helium in the LIC prior to interactions in the heliosphere remains open.

Interstellar magnetic fields may be important: Using *IBEX* observations of the circular shaped ribbon of intense emission by energetic neutral atoms, Zirnstein et al. (2016) derived the interstellar magnetic field strength of $2.93 \pm 0.08 \mu\text{G}$ outside of the heliosphere. The magnetic pressure of this field is comparable to the gas pressure in the heliopause leading to the magnetic field draping and altering the shape of the heliopause region. Also, the MHD calculations by Zank et al. (2013) show that for an interstellar magnetic field of this strength, the boundary between the outer heliopause and the interstellar medium will be a bow wave rather than a shock wave. At the center of the ribbon, the direction of this magnetic field is $\lambda = 227.28^\circ \pm 0.69^\circ$, $\beta = 34.62^\circ \pm 0.45^\circ$ in ecliptic coordinates or $l = 25.98^\circ \pm 0.70^\circ$, $b = 50.09^\circ \pm 0.57^\circ$ in Galactic coordinates. The 41 degree angle between the interstellar magnetic field and the inflow direction means that the magnetic field can change the apparent inflow direction of ions relative to the undeflected neutrals. The inflow direction of neutral hydrogen and helium atoms is not influenced by the magnetic field unless these neutrals had previously been ions before charge exchange. The consistent values of λ and β for He^0 measured by *IBEX* and *Ulysses* and for He^+ measured by *STEREO* suggest that magnetic fields may not play an important role in changing the inflow flow vector based on ionized and neutral helium, but this is an open question.

We conclude that the inflow and LIC vectors are different and that this difference indicates that the heliosphere is now passing through a region different from the main body of the LIC. The heliosphere may be inside the outer edge of the LIC with properties modified by EUV radiation or contact with ionized gas. Additional observations are needed to address this question.

7. SIGHTLINES TO NEARBY STARS

We now describe the placement of warm interstellar clouds and H II intercloud gas along the lines of sight (LOS) to nearby stars. Figure 10 shows the gas components along the sightlines to four nearby stars. The distance scales assume that $n(\text{H I})=0.2 \text{ cm}^{-3}$ (Slavin & Frisch 2008) for all of the partially ionized clouds. We require that α Cen, ϵ Eri, and other stars with detected astrospheric absorption are surrounded by partially ionized hydrogen clouds. With these constraints, we propose that the sightlines to nearby stars have the following structures:

- **The LOS to Sirius:** LIC and Blue are the two detected partially ionized clouds in this LOS. We propose that the LIC extends from the outer heliosphere to 0.25 pc in the direction of Sirius, followed by the Blue cloud for a distance of 0.25 pc, and then H II gas photoionized by Sirius B and ϵ CMa filling the remaining 2.14 pc to Sirius.
- **The LOS to α Cen:** Only the G cloud absorption is detected extending over a distance of 0.70 pc if we assume that $n(\text{H I})$ in the G cloud is same as in the LIC. The remaining 0.62 pc would filled with H II gas from Sirius B and ϵ CMa. Since α Cen has an astrosphere (Wood et al. 2002), it must be surrounded by gas containing neutral hydrogen, which we assume is the G cloud. However, heliospheric hydrogen wall absorption is detected in the direction of α Cen (Wood et al. 2005), implying that the outer heliosphere must be in contact with neutral hydrogen gas in this direction. One explanation is to assume that a very thin layer of the LIC provides the neutral hydrogen needed to create the hydrogen wall in this direction but with a hydrogen column density too small to be detected. Another explanation is to extend the G cloud all of the way to the outer heliosphere. This can be accomplished by reducing the assumed $n(\text{H I})$ in the G cloud to 0.11 cm^{-3} , half of the value of the LIC, but consistent with

variability, the precision of n_e measurements in the LISM (Redfield & Falcon 2008), and with the measured $\log N(\text{H I}) = 17.6$ to α Cen. Figure 11 shows this model.

- The LOS to ϵ Eri:** Spectra of ϵ Eri show absorption only at the LIC velocity, but the star has an astrosphere (Wood et al. 2002) and, therefore, must be located in a presently unknown cloud containing neutral hydrogen. The LIC fills 1.10 pc along this LOS leaving 2.12 pc to be filled with ionized gas. Since Sirius is located 4.88 pc from ϵ Eri and 3.40 pc from the midpoint of the LOS from the Sun to ϵ Eri, we do not expect that the H II gas produced by Sirius B can fill the missing 2.12 pc along the Sun- ϵ Eri LOS. Another hot white dwarf, 40 Eri B, is located 6.11 pc from ϵ Eri, but it is unlikely that its H II region gas comes close to the Sun- ϵ Eri LOS. Instead, ϵ CMa is the likely source for this ionized gas. The gas-pressure of the LIC, $(n_{\text{HI}} + n_e + n_p + n_{\text{He}})T = 2710 \text{ K cm}^{-3}$, where $n_{\text{HI}}=0.2 \text{ cm}^{-3}$, $n_e = n_p = 0.07 \pm 0.002 \text{ cm}^{-3}$ (Slavin & Frisch 2008), $n_{\text{He}}/n_{\text{H}} = 0.1$, and $T = 7500 \text{ K}$ (Redfield & Linsky 2008). If there is gas pressure balance between the LIC and the H II gas, then the temperature of the ionized gas along this LOS would be about 40,000 K.
- The LOS to Procyon:** Absorption by the LIC and beyond it the Aur cloud leave 1.25 pc of path length to be filled with ionized gas. The morphology of the Aur and other nearby clouds not in contact with the heliosphere will be the subject of a forthcoming paper. Ionizing radiation from Sirius B is the likely source of this ionized gas, since the separation of Sirius and Procyon is only 1.61 pc. This would be consistent with the gas temperature of about 7,500 K if there is gas-pressure balance between the extended H II region and the LIC.
- The LOS to π^1 UMa, V368 Cep, MN UMa, δ Dra, 47 Cas, and ι Cep:** Spectra of these stars centered near $l=130^\circ$, $b=+30^\circ$ with distances 14.4–35.4 pc all show interstellar absorption only at the LIC velocity with no evidence for any other neutral gas in the LOS. Since the LIC lies in the immediate vicinity of the Sun, the remainder of these lines of sight must be ionized gas. In addition to ϵ CMa, GJ3753 (14.1 pc) and especially the hot white dwarf G191-B2B (59.9 pc) may be responsible for much of the ionizing radiation from this general direction.

- **The LOS to 61 Vir, β Com, τ Boo, and χ Her:** Spectra of these stars, all located at high Galactic latitudes ($b > 44^\circ$), show interstellar absorption only by the NGP cloud with no evidence for absorption by the LIC or any other cloud. Since the closest star, 61 Vir ($d=8.53$ pc), likely has a detected astrosphere (Wood et al. 2005), the NGP cloud must be located near to and in front of this star and perhaps the other stars. This leaves about 6.8 pc of the LOS to 61 Vir and similar path lengths toward the other stars to be filled with ionized gas. The high Galactic latitude white dwarfs especially HZ 43 but also GJ3753, GJ433.1, and UZ Sex could provide part of this ionizing radiation in addition to that provided by ϵ CMa and β CMa.

Figure 11 is a schematic representation of the four partially ionized clouds that are in contact with the outer heliosphere as seen from the North Galactic pole. The figure shows the sight lines to 5 stars projected on to a plane parallel to the Galactic equator, and the length of each cloud located along each line of sight. Red shading indicates the Strömgren shells produced by EUV radiation from ϵ CMa. The direction of inflowing interstellar gas as seen from the Sun is at $b \approx 20^\circ$ where the LIC, Aql, and G clouds may be in contact.

8. COULD THE LISM CLOUDS IN CONTACT WITH THE HELIOSPHERE BE THE SOURCE OF ^{60}Fe ACCRETION?

With a half-life of 2.6 Myr, the radioisotope ^{60}Fe is produced during the very late evolution of massive stars and then ejected by supernovae into the interstellar medium. The presence of this isotope in deep ocean samples such as ferro-manganese crusts, nodules, and sediments (Knie et al. 1999; Wallner et al. 2016) and in the lunar regolith (Fimiani et al. 2016) indicates that supernovae have occurred within the last few Myr in the solar vicinity. Wallner et al. (2016) found evidence for enhanced ^{60}Fe accretion during the time intervals 1.5–3.2 Myr and 6.5–8.7 Myr ago but no evidence for ^{60}Fe accretion above background either more recently or outside of these two time intervals. They concluded that the ^{60}Fe detected during these two time intervals was produced by one or more supernovae occurring at these times. The most likely location for these supernovae would be in the

closest association of massive stars, the Scorpius-Centaurus Association at a distance of 100–150 pc. Within the Sco-Cen Association, the youngest star forming region where the recent supernova likely occurred is the Upper Scorpius region centered at $l = 352^\circ$ and $b = -15^\circ$. Fry, Fields, & Ellis (2015) concluded that the most likely explanation for the event timed at 2.2 My ago was the ejection of ^{60}Fe in the debris of an electron-capture supernova at a distance of about 100 pc and the subsequent condensation of the ^{60}Fe onto large ($> 0.2 \mu\text{m}$) interstellar grains. This could explain the amount of ^{60}Fe that arrived at Earth after traversing the interstellar medium and heliosphere.

Very recently, Koll et al. (2019) identified ^{60}Fe in dust grains embedded in Antarctic snow. After careful analysis, they concluded that the ^{60}Fe could not be explained by terrestrial nuclear explosions or by cosmogenic sources, but instead must have a supernova origin. Unlike the ocean core samples that were built up a long time ago, the Antarctic snow sample is a very recent accumulation over the last 20 years. The time scale for supernova debris to travel a distance of 100 pc through the interstellar medium would be about 200,000 yr (Fry, Fields, & Ellis 2015), which is much less than the half-life of ^{60}Fe or the time of the most recent supernovae and thus cannot directly explain the very recent accretion of ^{60}Fe .

Since iron is singly ionized in interstellar gas, iron ions flow around rather than penetrating the heliosphere. To reach the inner solar system, ^{60}Fe must, therefore, be included in interstellar grains. The large depletion of iron from the gas phase of LISM clouds requires that most of the iron is resident in dust grains that are likely olivine silicates (Redfield & Linsky 2008; Frisch, Redfield, & Slavin 2011). *In situ* measurements of interstellar dust by experiments on *Ulysses* and other spacecraft sample dust grains with sizes larger than about $0.3 \mu\text{m}$, because solar radiation pressure and heliospheric magnetic fields filter out most of the smaller grains (Mann 2010; Krüger et al. 2019). Larger grains are expected to reach the inner solar system without significant changes in direction or speed. In their analysis of data from the *Ulysses* impact ionization dust detectors, Strub, Krüger, & Sterken (2015) found that the speed ($\approx 26 \text{ km s}^{-1}$) of large dust grains (sizes greater than $0.5 \mu\text{m}$) and their flow toward ecliptic longitude $\lambda = 75^\circ \pm 30^\circ$ and latitude $\beta = -13^\circ \pm 4^\circ$ are similar to neutral helium gas in the LIC and other nearby clouds. The large uncertainty in λ precludes identification of the

dust flow with the helium gas flow of a specific cloud, but the the data are consistent with the dust flowing with the gas in the LIC, G, or other nearby clouds. Interstellar grains with sizes less than $1\mu\text{m}$ should be well coupled to the gas in warm clouds as the Larmor radius for electrically charged grains is $< 1\text{ pc}$ for an interstellar magnetic field of $5\text{ }\mu\text{G}$ (Grün & Landgraf 2000).

We propose two possible explanations for the recent arrival of interstellar dust grains containing ^{60}Fe in Antarctic snow. One is that the dust grains containing ^{60}Fe are resident in the warm LISM clouds and enter the heliosphere from one or all of the four clouds that are in contact with the outer heliosphere. The density of dust grains in the ionized intercloud medium should be much less than in the warm clouds because strong UV radiation and shocks can destroy grains and the low gas density means slower grain formation. Since the Sun is moving at a speed of 26.3 pc per million years through the cluster of local clouds, it entered the local cluster about 200,000 years ago and will leave in about the same time assuming that the warm clouds extend about 5 pc in all directions. This is a rough estimate, but it gives a time scale for the input of dust grains containing ^{60}Fe from a recent supernova. This scenario predicts continuous low level accretion of ^{60}Fe containing grains from warm clouds only when they are in contact with the heliosphere. This scenario can be tested by searching for ^{60}Fe deeper in snow and ice fields going back to more than 200,000 years.

An alternative explanation is that a large number of dust grains entered the heliosphere during the year 2005 when the measured flux of dust increased a factor of 3 and the inflow abruptly changed direction by $50^\circ \pm 7^\circ$ (Strub, Krüger, & Sterken 2015). This event might have been able to increase the terrestrial accretion rate to a level just above background and thus appear as a one-time occurrence. A possible scenario would be a change in which cloud is feeding dust grains into the heliosphere. The absence of detected ^{60}Fe dust grains above background deeper in snow and ice fields would be consistent with the recent detection being due to a one-time event.

New measurements are clearly needed to test between these two scenarios. As suggested by Koll et al. (2019) and by Fry, Fields, & Ellis (2015), future measurements of the ^{60}Fe dust particles located deeper in Antarctic snow/ice fields could provide a historical record of the Sun's motion through the LIC and other clouds in the LISM.

9. CONCLUSIONS AND FURTHER WORK

Observations and analysis of 62 sightlines with interstellar velocity components consistent with the Local Interstellar Cloud vector permitted us to compute a three-dimensional model of the LIC. This model extends from the heliosphere about 2 pc toward Galactic longitude $l = 135^\circ$ and latitude $b = +20^\circ$, but about 0 pc in the opposite direction ($l = 315^\circ$, $b = -20^\circ$). This peculiar shape, which has been identified in previous studies, highlights the question of whether the heliosphere is located inside or outside of the LIC. To better understand this question, we analyzed spectroscopic data and obtained the following results:

(1) As seen from the geometric center of the LIC, the distance to its edge is less than 0.5 pc within a wide solid angle defined by $225^\circ \leq l \leq 290^\circ$ and $-60^\circ \leq b \leq +10^\circ$. We call this region of minimal neutral hydrogen column density the “hydrogen hole”. Inside of the hydrogen hole are sight lines to the strongest source of EUV radiation (ϵ CMa), the second strongest source (β CMa), and the nearby hot white dwarf Sirius B. Photoionization of neutral hydrogen by the strong EUV radiation from these stars is the most likely cause of the hydrogen hole.

(2) Inside of the hydrogen hole, sight lines to eight stars show interstellar absorption by gas at the Blue cloud’s radial velocity but not at the predicted LIC velocity. The outline of the Blue cloud overlaps that of the hydrogen hole, indicating that the Blue cloud and the hydrogen hole are probably physically associated. We propose that the outer edge of the Blue cloud is a Strömgren shell being pushed against the outer heliosphere by higher ionized gas behind it. The outer layers of other clouds facing ϵ CMa are also Strömgren shells if they are not shielded by other clouds. The presence of Si III and likely C IV absorption in the sight lines to ϵ CMa and β CMa support the argument that these sight lines pass through Strömgren shells. The radial velocity and higher gas pressure of the Blue cloud are consistent with compression. Since the flow vector of interstellar gas inside of the hydrogen hole differs substantially from that of main body of the LIC, the heliosphere lies outside of the LIC in this direction.

(3) The vector of interstellar gas flowing into the heliosphere as measured by the *IBEX*, *Ulysses*, and *Stereo* spacecraft differs from that inferred from interstellar absorption lines representing the flow

of LIC gas far from the heliosphere at a distance of roughly 1 pc. This difference of $2\text{--}3 \text{ km s}^{-1}$ in speed and slightly different direction, should be tested by precise new measurements. We conclude that the inflow and LIC vectors are different and propose that this difference indicates that the heliosphere is now passing through a region different from the main body of the LIC. The heliosphere could be inside the outer edge of the LIC where the flow is modified by EUV radiation. Additional observations are needed to address this question.

(4) We propose a model for LISM immediately outside of the heliosphere. The presence of heliospheric hydrogen wall absorption in all directions requires that the outer heliosphere be in contact with and be surrounded by interstellar gas containing a significant amount of neutral hydrogen. In the hydrogen hole region, the Blue cloud is in direct contact with the outer heliosphere. At the edge of the hydrogen hole, the LIC is in contact with the outer heliosphere with the Blue cloud lying immediately outside of the LIC. Away from the hydrogen hole toward higher Galactic longitudes, the Aql cloud is in direct contact with the outer heliosphere. In the direction of α Cen, there must be partially ionized gas in contact with both the heliosphere and the astrosphere. We adopt a model in which the G cloud fills this entire line of sight to the star with neutral hydrogen density $n(\text{H I}) \approx 0.11 \text{ cm}^{-3}$, although a very thin layer of LIC gas may be in contact with the heliosphere in this direction. For $l = 90^\circ - 235^\circ$, the LIC is in contact with the outer heliosphere. Our model with the heliosphere in direct contact with four interstellar clouds may result from the directionality of the EUV radiation from ϵ CMa. The different kinematics of the partially ionized interstellar gas clouds may result from whether a cloud receives direct ionizing radiation or is shielded by other clouds now and in the recent past. The complex magnetic field surrounding the heliosphere may also play a role in determining the shape and properties of these clouds.

(5) We describe the lines of sight to nearby stars in terms of several partially ionized clouds and H II gas which has been photoionized by the EUV radiation from ϵ CMa and other stars. The modest degree of ionization in the nearby intercloud gas and the strong EUV radiation field suggest that the intercloud gas is an irregularly shaped Strömgren sphere rather than a recombining plasma following a supernova shock.

(6) Finally, we note that the heliosphere is leaving a region of space where the LIC, G, Aql, and Blue clouds are located. We propose that the very recent measurement in Antarctic snow of enhanced ^{60}Fe from the debris of a supernova could be explained by the inflow of interstellar grains containing ^{60}Fe from the warm clouds in contact with the heliosphere either continuously at a low level or during an unusual event.

Our models for the LIC morphology and the very local ISM are updates of our previous studies (Redfield & Linsky 2000, 2008). In a subsequent paper, we will present the results of a new three-dimensional LISM model including data studied by Malamut et al. (2014) and more recently observed sightlines. When this is available, we will reexamine the extent to which stellar EUV radiation may explain the properties of the intercloud gas between the LISM.

We acknowledge support through the NASA HST Grant GO-11568 from the Space Telescope Science Institute, which is operated by the Association of Universities for Research in Astronomy, Inc. for NASA, under contract NAS 5-26555. Support for *HST* observing programs #11568 was provided by NASA through a grant from the Space Telescope Science Institute. We thank John Vallergera for a very thoughtful referee report, Martin Barstow for computing the ionizing flux from Sirius B, and Steven Burrows for his graphics. JLL thanks the Erwin Schrödinger International Institute for Mathematics and Physics at the University of Vienna for their hospitality and opportunity to learn about nucleosynthetic isotope anomalies. Our research has made use of NASA's Astrophysics Data System Bibliographic Services and the SIMBAD database, operated at CDS, Strasbourg, France.

Facilities: HST (GHRS, STIS), FUSE, EUVE, CHIPS, ULYSSES

REFERENCES

- | | |
|--|---|
| Barstow, M. A., Bond, H. E., Holberg, J. B.,
Burleigh, M. R., Hubeny, I., & Koester, D.
2005, MNRAS, 362, 1134 | Barstow, M. A., Boyce, D. D., Welsh, B. Y.,
Lallement, R., Barstow, J. K., Forbes, A. E., &
Preval, S. 2010, ApJ, 723, 1762 |
| | Berghöfer, T. W. & Breitschwerdt, D. 2002, A&A,
390, 299 |

- Bertin, P., Vidal-Madjar, A., Lallement, R.,
Ferlet, R., & Lemoine, M. 1995, A&A, 302, 889
- Breitschwerdt, D., Schmutzler, T. 1999, A&A,
347, 650
- Bzowski, M., Swaczyna, P., Kubiak, M. A.; Sokół,
J. M., Fuselier, S. A., Galli, A., Heirtzler, D.,
Kucharek, H., Leonard, T. W., McComas, D. J.,
et al. 2015, ApJS, 220, 28
- Chassefiere, E., Bertaux, J. L., Lallement, R.,
Kurt, V. G. 1986, A&A, 160, 229
- Cox D. P. in *The Local Bubble and Beyond* ed. D.
Breitschwerdt, M. J. Freyberg & Trümper, J.
1998, IAU Coll. 166, Lecture Notes in Physics,
506, 121
- Cravens, T. E. 1997, GeoRL, 24, 105
- Crutcher, R. M. 1982, ApJ, 254, 82
- Dring, A. R., Linsky, J., Murthy, J., Henry, R. C.,
Moos, W., T Vidal-Madjar, A., Audouze, J., &
Landsman, W. 1997, ApJ, 488, 760
- Dupin, O. & Gry, C. 1998, A&A, 335, 661
- Dupuis, J., Vennes, S., Bowyer, S., Pradhan,
A. K., & Thejll, P. 1995, ApJ, 455, 574
- Edelstein, J., Bowyer, S., Korpela, E. J.,
Lampton, M., Trapero, J., Gómez, J. F.,
Morales, C., Orozco, V. 2001, Ap&SS, 276, 177
- Ferlet, R., Lecavelier des Etangs, A.,
Vidal-Madjar, A., Bertin, P., Deleuil, M.,
Lagrange-Henri, A., & Lallement, R. 1995,
A&A, 297, L5
- Field, G. B., Goldsmith, D. W., & Habing, H. J.
1969, ApJL, 155, L149
- Fimiani, L., Cook, D.L., Faestermann, T., et al.
2016, PhRvL, 116, 151104
- Frisch, P. C., Bzowski, M., Drews, C., Leonard,
T., Livadiotis, G., McComas, D. J., Möbius, E.,
Schwadron, N., Sokół, J. M. 2015, ApJ, 801, 61
- Frisch, P. C., Bzowski, M., Livadiotis, G., et al.
2013, Science, 341, 1080
- Frisch, P.C., Redfield, S., & Slavin, J.D. 2011,
ARA&A, 49, 237
- Frisch, P. C., Grodnicki, L. & Welty, D. E. 2002,
ApJ, 574, 834
- Frisch, P.,C., Redfield, S. & Slavin, J. D. 2011,
ARA&A, 49, 237
- Fry, B.J., Fields, B.D., & Ellis, J.R. 2015, ApJ,
800, 71
- Galeazzi, G. M., Chiao, M., Collier, M. R., et al.
2014, Nature, 512, 171
- Gloeckler, G., Möbius, E., Geiss, J., et al. 2004,
A&A, 426, 845
- Grün, E., & Landgraf, M. 2000, J. Geophys. Res.,
105, 10291
- Gry, C., Jenkins, E. B. 2014, A&A, 567, 58
- Gry, G., Lemonon, L., Vidal-Madjar, A., Lemoine,
M., & Ferlet, R. 1995, A&A, 302, 497
- Harwit, M. 1988, *Astrophysical Concepts* (New
York: Springer-Verlag)
- Hébrard, G., Mallouris, C., Ferlet, R., Koester, D.,
Lemoine, M., Vidal-Madjar, A., & York, D.
1999, A&A, 350, 643
- Hurwitz M., Sasseen, T. P. & Sirk, M. M. 2005,
ApJ, 623, 911

- Jenkins, E. B., Gry, C., Dupin, O. 2000, *A&A*, 354, 253
- Knie, K., Korschinek, G., Faustermann, T., et al. 1999, *PhRvL*, 83, 18
- Koll, D., Korschinek, G., Faustermann, T., et al. 2019, *PhRvL*, 123, 072701
- Koutroumpa, D. 2012, *Astron. Nachr.*, 333, 341
- Koutroumpa, D., Lallement, R., Raymond, J. C., & Kharchenko, V. 2009, *A&A*, 696, 1517
- Koutroumpa, D., Quémerais, E., Katushkina, O., Lallement, R., Bertaux, J.-L., & Schmidt, W. 2017, *A&A*, 598, A12
- Krüger, H., Strub, P., Altobelli, N., Sterken, V.J., Srama, R., & Grün, E. 2019, *A&A*, 626, A37
- Kubiak, M. A., Bzowski, M., Sokół, J. M., Swaczyna, P., Grzedzielski, S., Alexashov, D.B., Izmodenov, V. V., Möbius, E., Leonard, T., Fuselier, S. A., et al. 2014 *ApJS*, 213,29
- Kubiak, M. A., Swaczyna, P., Bzowski, M., Sokół, J. M., Fuselier, S. A., Galli, A., Heirtzler, D., Kucharek, H., Leonard, T. W., McComas, D. J. 2016, *ApJS*, 223, 25
- Lallement, R. & Bertaux, J.-L. 2014, *A&A*, 565, A41
- Lallement, R. & Bertin, P. 1992, *A&A*, 266, 479
- Lallement, R., & Ferlet, R. 1997, *A&A*, 324, 1105
- Lallement, R., Ferlet, R., Lagrange, A. M., Lemoine, M., & Vidal-Madjar, A. 1995, *A&A*, 304, 461
- Lallement, R., Quémerais, E., Bertaux, J. L., Ferron, S., Koutroumpa, D., & Pellinen, R. 2005, *Science*, 307, 1447
- Lecavelier des Etangs, A., Deleuil, M., Vidal-Madjar, A., Lagrange-Henri, A., Backman, D., Lissauer, J. J., Ferlet, R., Beust, H., & Mouillet, D. 1997, *A&A*, 325, 228
- Leonard, T. W.; Möbius, E., Bzowski, M., Fuselier, S. A., Heirtzler, D., Kubiak, M. A., Kucharek, H., Lee, M. A., McComas, D. J., Schwadron, N. A., & Wurz, P. 2015, *ApJ*, 804, 42
- Linsky, J. L., Diplas, A., Wood, B. E., Brown, A., Ayres, T. R., & Savage, B. D. 1995, *ApJ*, 451, 335
- Linsky, J. L., Draine, B. T., Moos, H. W., et al. 2006, *ApJ*, 647, 1106
- Lisse, C. M., Dennerl, K., Englhauser, J., Harden, M., Marshall, F. E., Mumma, M. J., Petre, R., Pye, J. P., Ricketts, M. J., Schmitt, J., et al. 1996, *Science*, 274, 205
- Lyu, C.-H., Bruhweiler, F. C. 1996, *ApJ*, 459, 216
- Malamut, C., Redfield, S., Linsky, J. L., Wood, B. E., & Ayres, T. R. 2014, *ApJ*, 787, 75
- Mann, I. 2010, *ARA&A*, 48, 173
- McComas, D. J., Alexashov, D., Bzowski, M., et al. 2012, *Science*, 336, 1291
- McComas, D. J., Bzowski, M., Fuselier, S. A., Frisch, P. C., Galli, A., Izmodenov, V. V., Katushkina, O. A., Kubiak, M. A., Lee, M. A., Leonard, T. W., et al. 2015 *ApJS*, 220, 22
- McCullough, P. R. 2000, *PASP*, 112, 1542
- McKee, C. F., & Ostriker, J. P. 1977, *ApJ*, 218, 148

- Metchev, S. A., & Hillenbrand, L. A. 2009, *ApJS*, 181, 62
- Möbius, E., Bochslers, P., Bzowski, M., et al. 2012, *ApJS*, 198, 11
- Möbius, E., Bzowski, M., Frisch, P. C., Fuselier, S. A., Heirtzler, D., Kubiak, M. A., Kucharek, H., Lee, M. A., Leonard, T., & McComas, D. J. 2015a, *ApJS*, 220, 24
- Möbius, E., Lee, M. A., Drews, C. 2015b, *ApJ*, 815, 20
- Peek, J. E. G., Heiles, C., Peek, K. M. G., Meyer, D., & Lauroesch, J. T. 2011, *ApJ*, 735, 129
- Piskunov, N., Wood, B. E., Linsky, J. L., Dempsey, R. C., & Ayres, T. R. 1997, *ApJ*, 474, 315
- Quemerais, E., Bertaux, J., Sandel, B. R., & Lallement, R. 1994, *A&A*, 290, 941
- Redfield, S., & Falcon, R. E. 2008, *ApJ*, 683, 207
- Redfield, S., & Linsky, J. L. 2000, *ApJ*, 534, 825
- Redfield, S., & Linsky, J. L. 2001, *ApJ*, 551, 413
- Redfield, S., & Linsky, J. L. 2002, *ApJS*, 139, 439
- Redfield, S., & Linsky, J. L. 2004a, *ApJ*, 602, 776
- Redfield, S., & Linsky, J. L. 2004b, *ApJ*, 613, 1004
- Redfield, S., & Linsky, J. L. 2008, *ApJ*, 673, 283
- Redfield, S., Linsky, J. L. 2015, *ApJ*, 812, 125
- Robertson, I. P., Cravens, T. E. 2003, *J. Geophys. Res.*, 108(A10), 8031
- Slavin, J. D. & Frisch, P. C. 2008, *A&A*, 491, 53
- Snowden, S. L., Chiao, M., Collier, M. R. 2014b, *ApJ*, 791, L14
- Snowden, S. L., McCammon, D., Burrows, D. N., & Mendenhall, J. A. 1994, *ApJ*, 424, 714
- Strömgren, B. 1939, *ApJ*, 89, 526
- Strub, P., Krüger, H., & Sterken, V.J. 2015, *ApJ*, 812, 140
- Swaczyna, P., Bzowski, M., Kubiak, M. A., et al. 2018, *ApJ*, 854, 119
- Tat, H. T. & Terzian, Y. 1999, *PASP*, 111, 1258
- Taut, A., Berger, L., Möbius, E., Drews, C., Heidrich-Meisner, V., Keilbach, D., Lee, M. A., Wimmer-Schweingruber, R. F. 2018, *A&A*, 611, 61
- Vallerga, J. 1998, *ApJ*, 497, 921
- Vallerga, J., Lallement, R., Lemoine, M., Dalaudier, F., & McMullin, D. 2004, *A&A*, 426, 855
- Vallerga, J. V. & Welsh, B. Y. 1995, *ApJ*, 444, 702
- Vennes, S., Polonski, E. F., Lanz, T., Thorstensen, J. R., Chayer, P., & Gull, T. R. 2000, *ApJ*, 544, 423
- Wallner, A., Feige, J., Kinoshita, N., et al. 2016, *Nature*, 532, 69
- Welsh, B. Y., & Lallement, R. 2010, *PASP*, 122, 1320
- Welsh, B. Y., Sfeir, D., Sirk, M., & Lallement, R. 1999, *A&A*, 352, 308
- Welsh, B. Y. & Shelton, R. L. 2009, *Astrophys Space Sci.*, 323, 1
- Welsh, B. Y., Vallerga, J. V., & McDonald, K. 1998, *PASP*, 110, 827
- Welsh, B. Y., Wheatley, J., Dickinson, N. J., & Barstow, M. A. 2013, *PASP*, 125, 644
- Wolfire, M., McKee, C., Hollenbach, D., & Tielens, A. 1995, *ApJ*, 453, 673

- Wood, B. E., Alexander, W. R., & Linsky, J. L. 1996, *ApJ*, 470, 1157
- Wood, B. E., Ambruster, C. W., Brown, A., & Linsky, J. L. 2000, *ApJ*, 542, 411
- Wood, B. E., Izmodenov, V. V., Alexashov, D. B., Redfield, S., & Edelman, E. 2014a, *ApJ*, 780, 108
- Wood, B. E., & Linsky, J. L. 1998, *ApJ*, 492, 788
- Wood, B. E., Müller, H.-R., Redfield, S., & Edelman, E. 2014b, *ApJL*, 781, L33
- Wood, B. E.; Müller, H.-R., Witte, M. 2015, *ApJ*, 801, 62
- Wood, B. E., Müller, H.-R., Zank, G. P., & Linsky, J.L. 2002, *ApJ*, 574, 412
- Wood, B. E., Redfield, S., Linsky, J. L., Müller, H.-R. & Zank, G.P. 2005, *ApJS*, 159, 118
- Yorke, H. W. 1986, *ARA&A*, 24, 49
- Zachary, J., Redfield, S., Linsky, J. L., Wood, B. E. 2018 *ApJ*, 859, 42
- Zank, G. P., Heerikhuisen, J., Wood, B. E., Pogorelov, N. V., Zirnststein, E., McComas, D. J. 2013 *ApJ*, 763, 20
- Zirnststein, E. J., Heerikhuisen, J., Funsten, H. O., Livadiotis, G., McComas, D. J., Pogorelov, N. V. 2016, *ApJL*, 818, L18

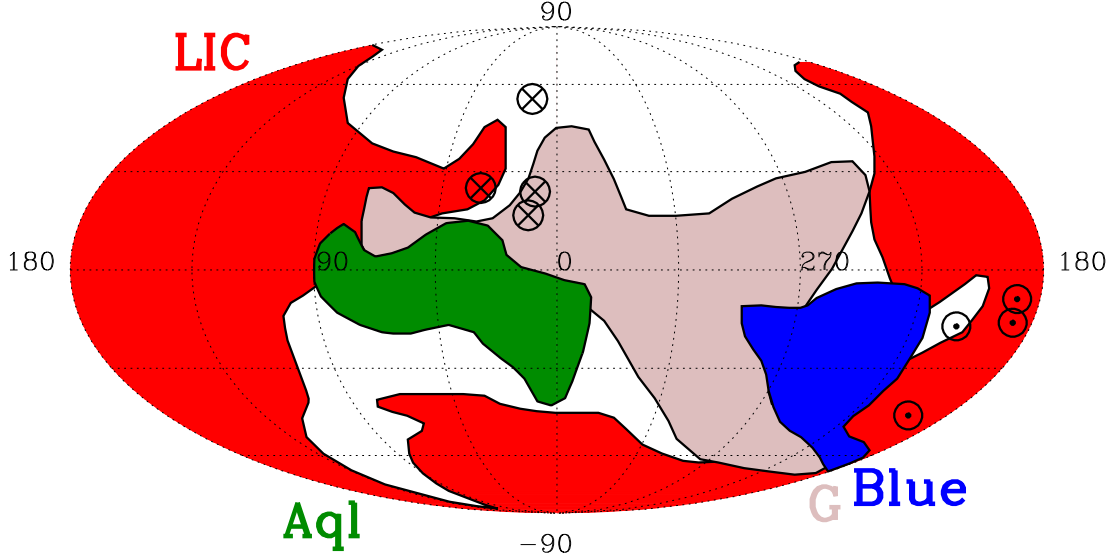


Figure 1. Morphologies of the four partially ionized LISM clouds that are in contact with the outer heliosphere. They are the LIC (red), which lies in front of ϵ Eri (3.2 pc), the G cloud (brown), which lies in front of α Cen (1.32 pc), the Blue cloud (dark blue), which lies in front of Sirius (2.64 pc), and the Aql cloud (green), which lies in front of 61 Cyg (3.5 pc). The plot is in Galactic coordinates with the Galactic Center direction in the center. The upwind direction of the LIC velocity vector is indicated by the circled-cross symbol near $l = 15^\circ$ and $b = +20^\circ$, and the upwind directions of the other clouds have similar marks. The downwind directions are indicated by the circled-dot symbols.. A full map of all 15 LISM clouds is given by [Redfield & Linsky \(2008\)](#).

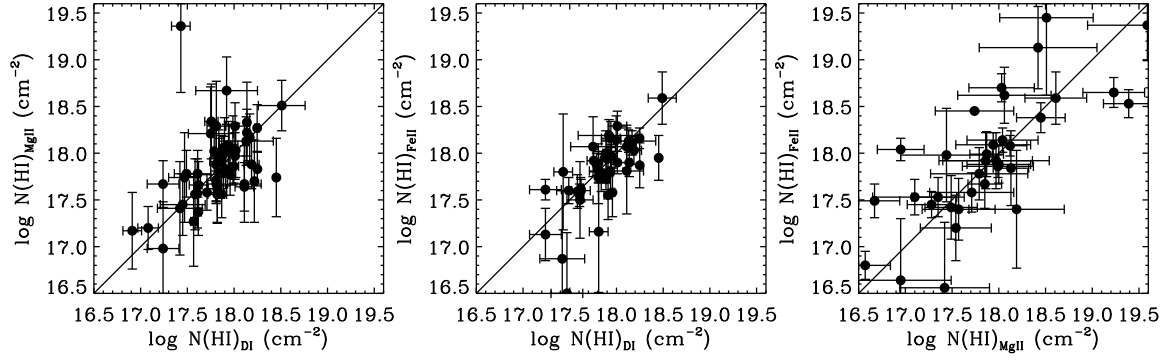


Figure 2. Comparison of H I column densities based on observed D I, Mg II, and Fe II column densities.

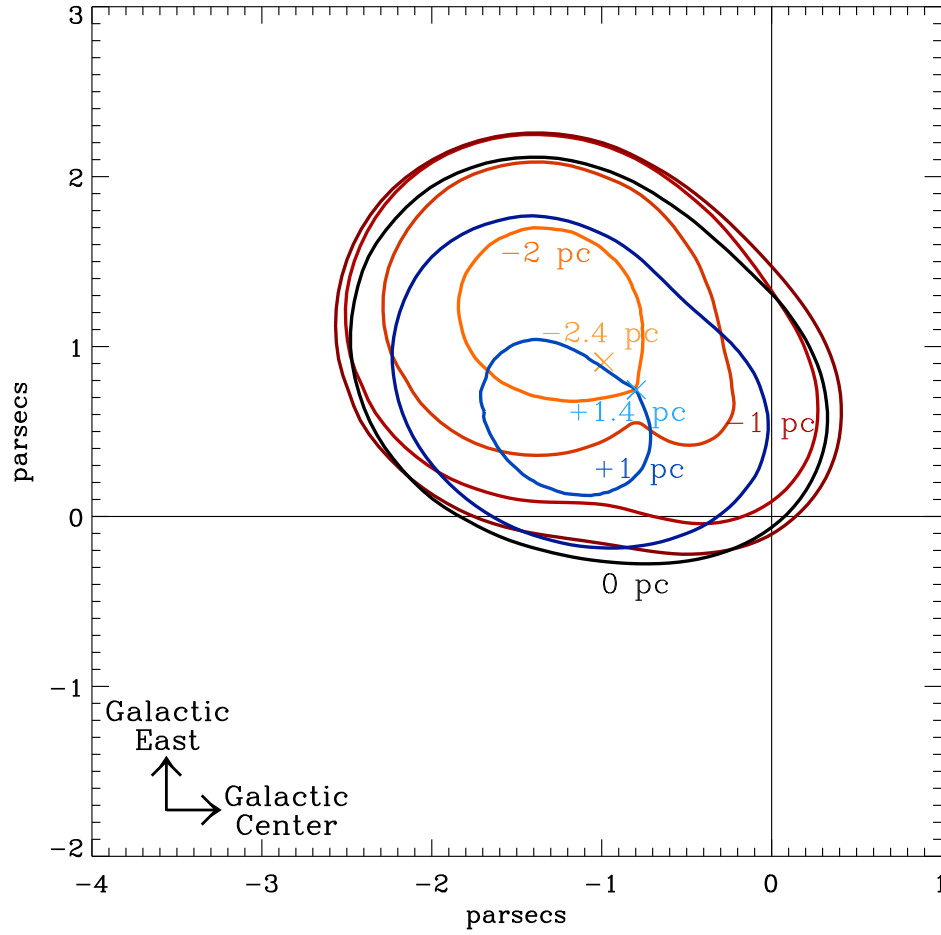


Figure 3. Contour map of LIC as viewed from North Galactic Pole. The Sun is located at the origin (0,0). Red contours are cuts above the LIC center parallel to the Galactic plane, and the blue contours are cuts below. The X symbols indicate the locations where the edge of the LIC is furthest above and below the plane of the figure.

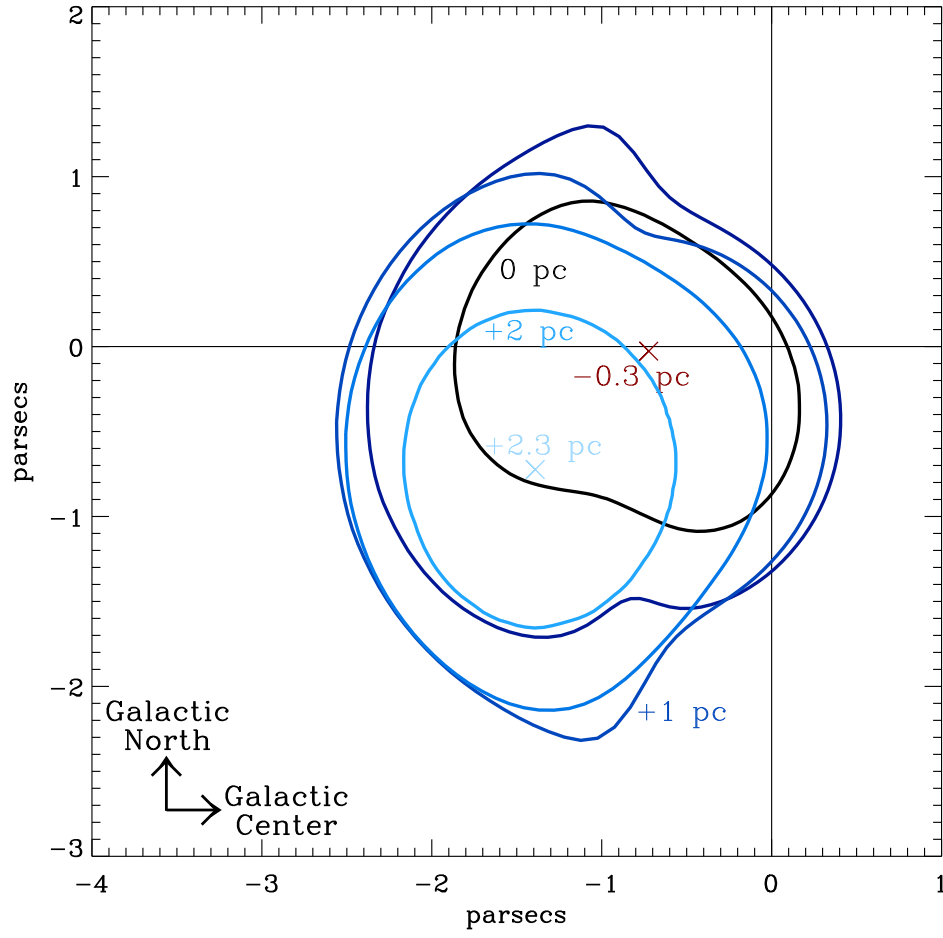


Figure 4. Contour map of LIC as viewed from Galactic East.

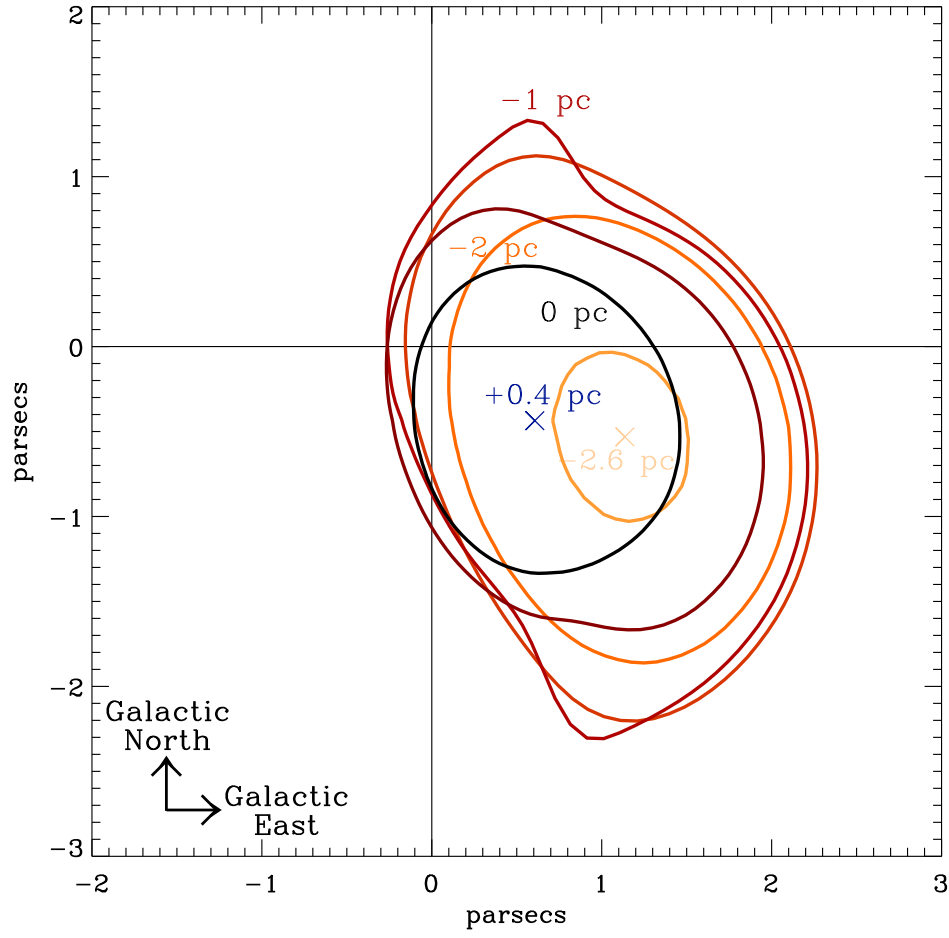


Figure 5. Contour map of LIC as viewed from the Galactic Center.

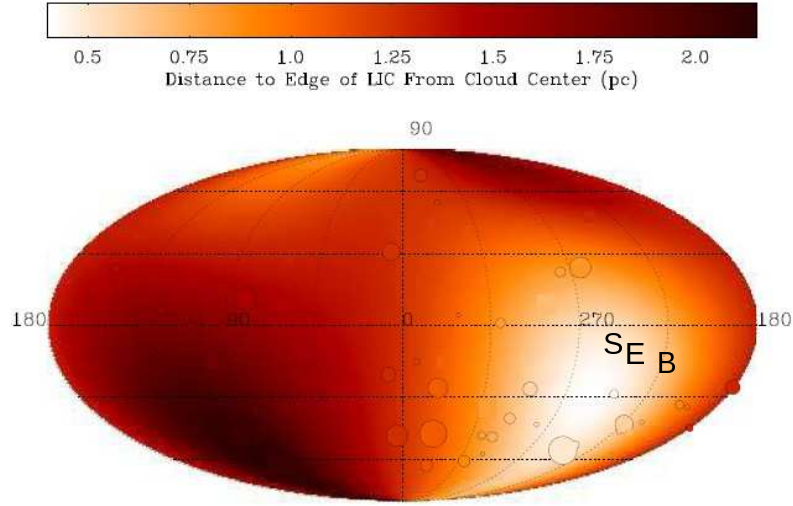


Figure 6. Distances to the edge of the LIC from its geometric center computed from $N(\text{H I})$ along lines of sight to 62 nearby stars. The symbols are S for the Galactic coordinates of the hot white dwarf Sirius B, E for ϵ CMa, and B for β CMa. Faint circles indicate the locations of stars near the hydrogen hole.

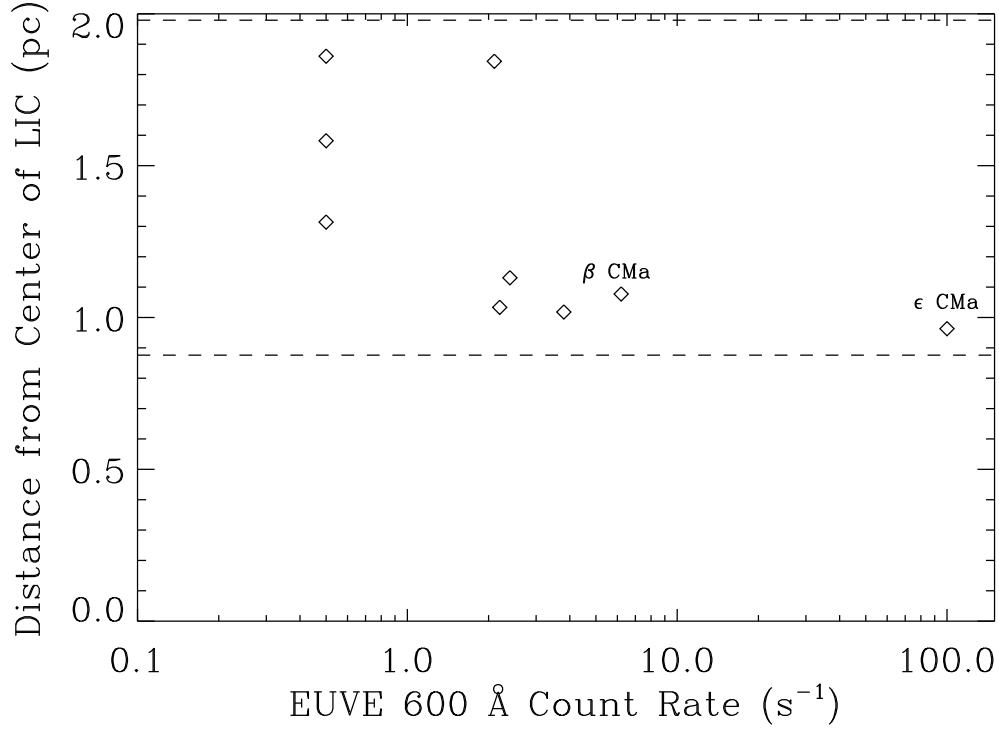


Figure 7. Distance from geometric center of the LIC to its edge along the lines of sight to the brightest EUV targets observed by *EUVE*. (Vallerga & Welsh 1995). The x-axis data are count rates measured through the wide band Tin filter centered near 600 Å. The sight lines to the brightest EUV sources (ϵ CMa at the far right and β CMa) have among the shortest path lengths to the center of the LIC. The dashed lines indicate the minimum and maximum path lengths from the geometric center of the LIC to its edge.

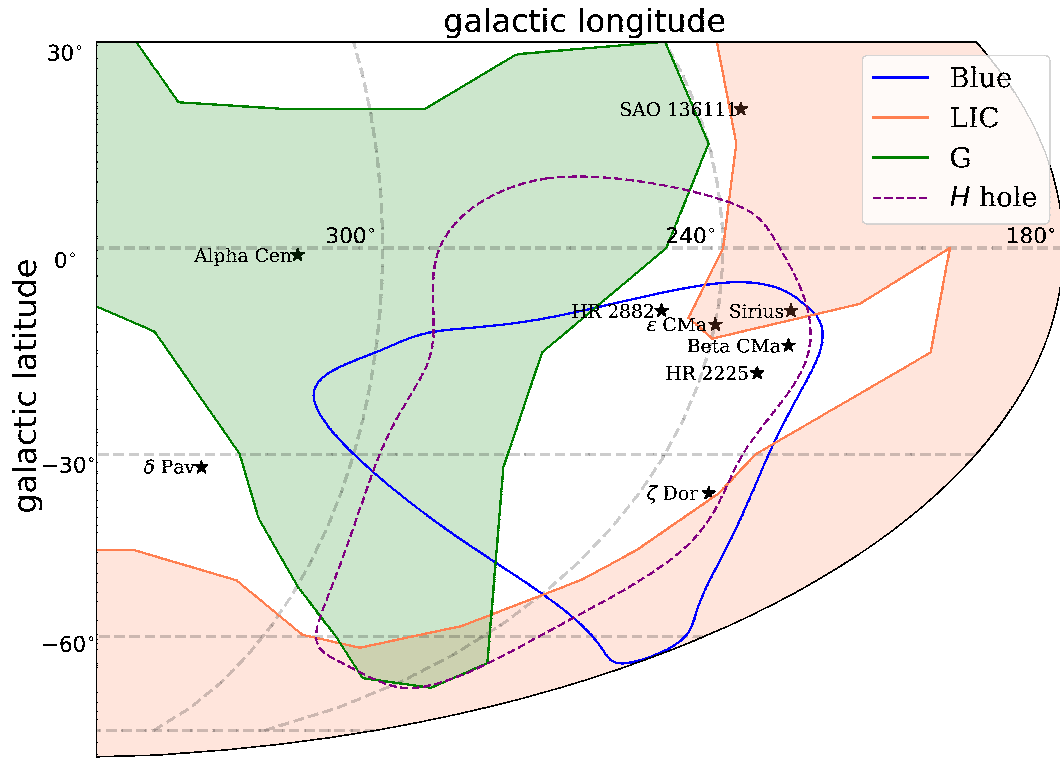


Figure 8. Outer edges of the hydrogen hole (dashed line) and the Blue clouds (blue solid line) in Galactic coordinates. Also shown are the locations of the LIC (peach) and G (green) clouds. The plotted stars are those with individual clouds observed in their lines of sight and (in many cases) knowledge of whether the solar hydrogen wall has been detected or not detected.

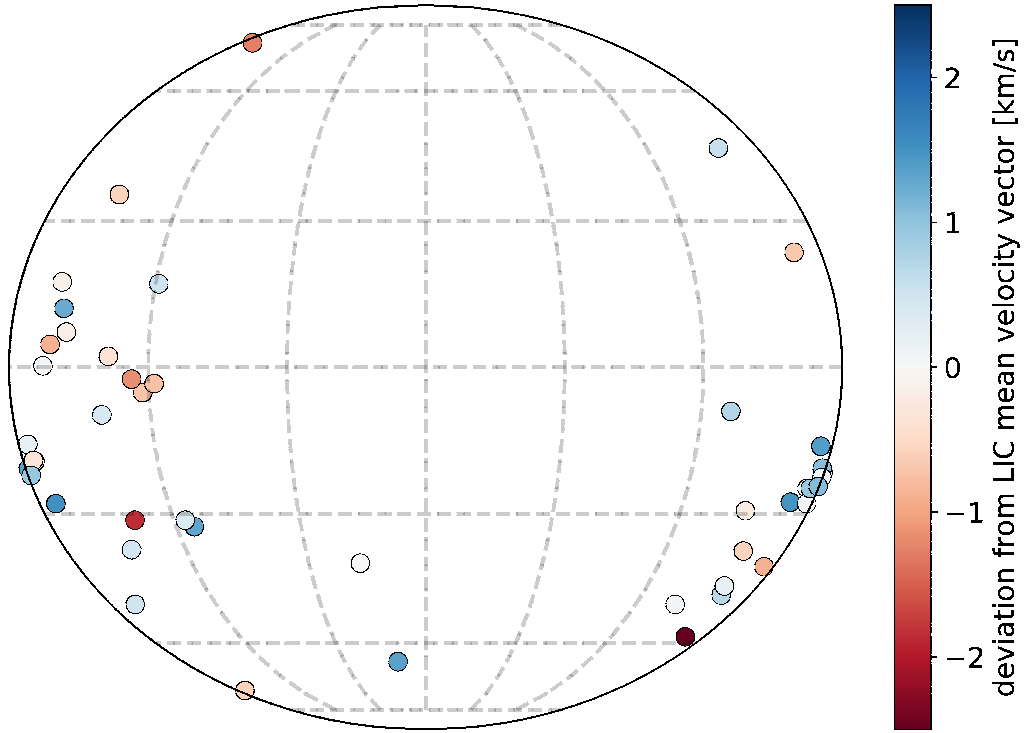


Figure 9. Radial velocity deviations from the LIC mean velocity vector for LIC velocity components in the lines of sight to 45 stars. The data are plotted in Galactic Coordinates.

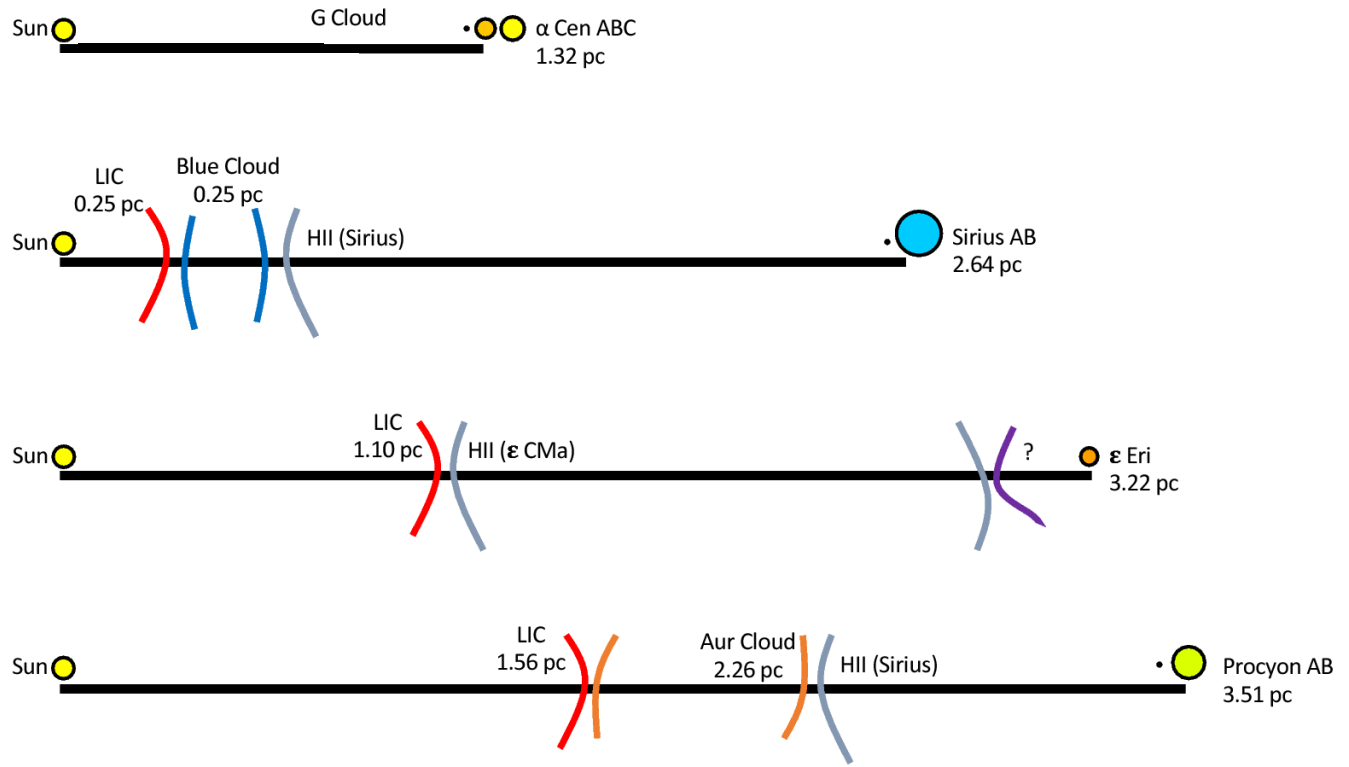


Figure 10. Interstellar gas components along the lines of sight to four stars within 4 pc of the Sun. These lines of sight include contributions from the LIC, G, Blue, and Aur clouds and the H II regions produced by EUV radiation from Sirius B and ϵ CMa.

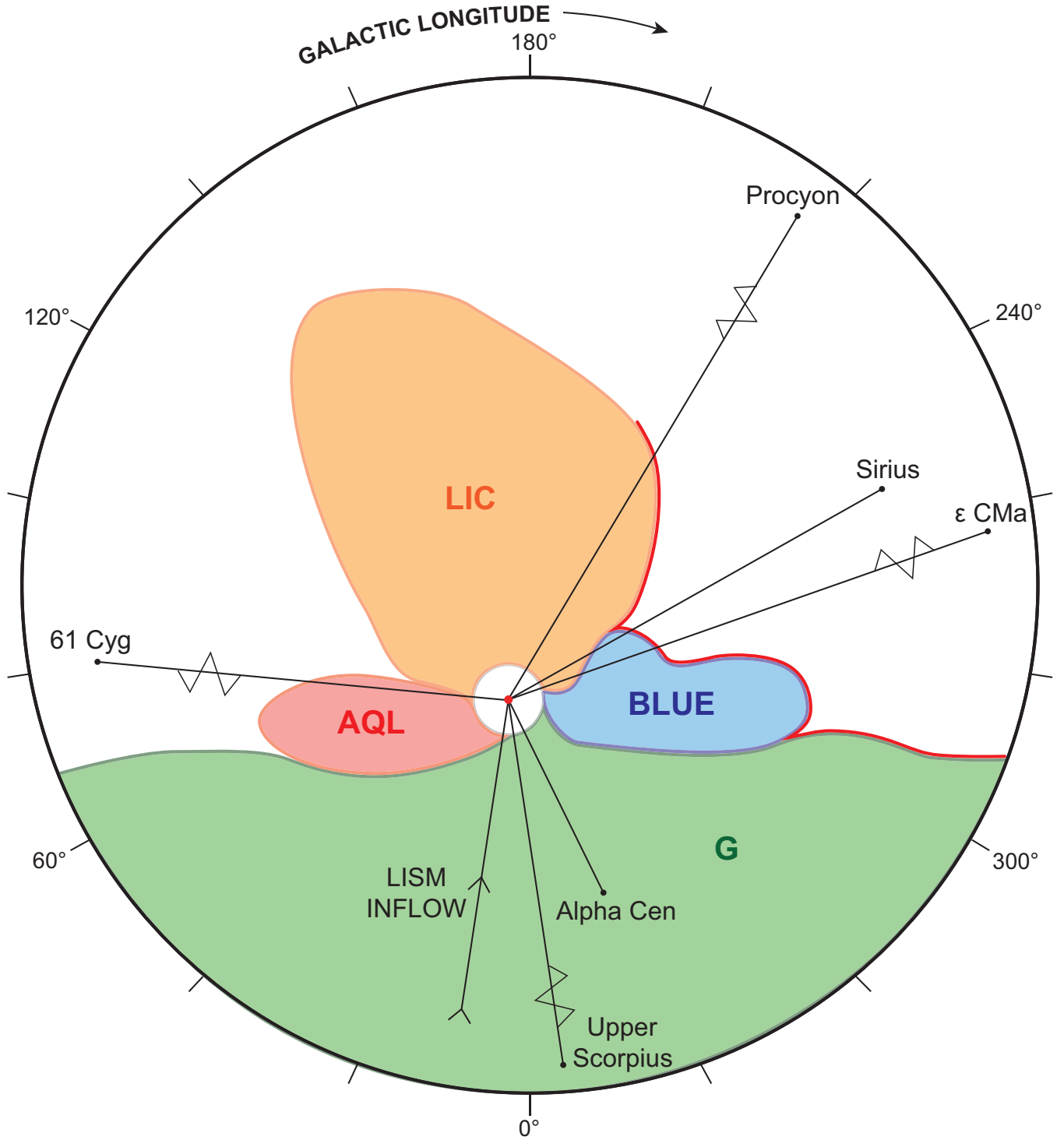


Figure 11. The local ISM region within 3 pc of the Sun as viewed from the North Galactic pole showing the location of the four partially ionized clouds that are in contact with the outer heliosphere. Not shown are other clouds lying outside of the four clouds. Shown are the Sun (point), an exaggerated representation of the heliopause (circle around the Sun) and the LIC, G, Aql, and Blue clouds. Lines of sight projected on to the Galactic equator are shown for 5 stars. Red shading shows the Strömgren shells produced by EUV radiation from ϵ CMa. Also shown are the direction of inflowing interstellar gas as seen from the Sun and the direction to the Upper Scorpius region of the Scorpius-Centauri Association where the most recent supernovae likely occurred.

Table 1. Heliospheric and astronomical measurements of inflowing LISM gas

Source	Method	v_{LISM} (km s $^{-1}$)	T (K)	λ (ecliptic)	β (ecliptic)	Ref. ^a
<i>EUVE</i>	He 0	24.5 ± 2	6500 ± 2000	74.7 ± 0.5	-5.7 ± 0.5	1
<i>IBEX</i>	He 0	26	8710^{+440}_{-680}	75.75 ± 0.92	-5.29 ± 0.05	2
<i>IBEX</i>	He 0	27.0 ± 1.3		74.5 ± 1.7	-5.2 ± 0.3	3
<i>IBEX</i>	He 0	25.76 ± 0.4	7440 ± 260	75.75 ± 0.5	-5.16 ± 0.10	4
<i>IBEX</i>	He 0	26.21 ± 0.37	7691 ± 230	75.41 ± 0.40	-5.03 ± 0.07	5
<i>Ulysses</i>	He 0	26.08 ± 0.21	7260 ± 270	75.54 ± 0.19	-5.44 ± 0.24	6
<i>STEREO</i>	He $^+$ PUI			75.21 ± 0.04		7
<i>STEREO</i>	He $^+$ PUI			75.41 ± 0.34		8
LIC cloud	H 0	23.84 ± 0.90	7500 ± 1300	78.53 ± 3.4	-7.20 ± 3.3	9
LIC cloud	H 0	23.9		78.6	-7.0	10
G cloud	H 0	29.6 ± 1.1	5500 ± 400	71.11 ± 1.9	-8.52 ± 3.6	9
Blue cloud	H 0	13.89 ± 0.89	3900 ± 2300	79.09	-26.60	9
<i>SWAN</i>	H 0	22 ± 1	11500 ± 1000	72.5	-8.8	11
<i>Ulysses</i>	dust	26		75 ± 30	-13 ± 4	12

^a(1) Vallergera et al. (2004); (2) Möbius et al. (2015a); (3) Leonard et al. (2015); (4) Bzowski et al. (2015); (5) Swaczyna et al. (2018); (6) Wood et al. (2015); (7) Möbius et al. (2015b); (8) Taut et al. (2018); (9) Redfield & Linsky (2008); (10) This paper; (11) Lallement et al. (2005); (12) Strub, Krüger, & Sterken (2015).

Table 2. LIC Cloud Sight Line Properties

Star	HD	l	b	d	v	$\log N(\text{Ion})$	Ion	Reference	$\log N(\text{H I})$	$d_{\text{dis}}^{\text{edge}}$	$d_{\text{cloud}}^{\text{edge}}$	σ^a
Name	#	(deg)	(deg)	(pc)	(km s $^{-1}$)	(cm $^{-2}$)			(cm $^{-2}$)	(pc)	(pc)	
α CMa A	48915	227.2	-8.9	2.64	18.55	12.43 ± 0.17	DI	1	17.24 ± 0.17	0.28 ± 0.11	0.24	0.4
α CMa B	48915B	227.2	-8.9	2.64	17.60	12.81 ± 0.10	DI	2	17.62 ± 0.10	0.67 ± 0.16	0.24	2.8
ϵ Eri	22049	195.8	-48.1	3.22	18.73	13.03 ± 0.06	DI	3	17.837 ± 0.061	1.11 ± 0.16	0.91	1.3
α CMi	61421	213.7	13.0	3.51	19.76	13.08 ± 0.04	DI	4	17.887 ± 0.042	1.25 ± 0.12	0.38	7.3
ϵ Ind	209100	336.2	-48.0	3.62	-9.20	13.20 ± 0.10	DI	5	18.01 ± 0.05	1.65 ± 0.38	0.13	4.0
τ Cet	10700	173.1	-73.4	3.65	12.34	13.182 ± 0.002	DI	6	17.989 ± 0.011	1.58 ± 0.32	1.18	1.2
40 Eri A	26965	200.8	-38.1	4.98	21.73	13.03 ± 0.1	DI	7	17.84 ± 0.10	1.11 ± 0.26	0.79	1.3
η Cas A	4614	122.6	-5.1	5.95	11.18	12.43 ± 0.09	FeII	8	18.10 ± 0.14	2.04 ± 0.67	2.63	-0.9
α Lyr	172167	67.5	19.2	7.68	-12.90	13.03 ± 0.1	FeII	9	18.70 ± 0.15	8.1 ± 2.8	0.63	2.7
α PsA	216956	20.5	-64.9	7.70	-5.87	12.58 ± 0.1	FeII	10	18.25 ± 0.15	2.9 ± 1.0	0.57	2.3
χ^1 Ori	39587	188.5	-2.7	8.66	23.08	12.98 ± 0.01	DI	8	17.787 ± 0.015	0.992 ± 0.034	1.35	-10.5
δ Eri	23249	198.1	-46.0	9.04	19.60	13.056 ± 0.007	DI	6	17.863 ± 0.013	1.18 ± 0.24	0.86	1.3
CF UMa	103095	168.5	73.8	9.09	2.05	12.58 ± 0.14	MgII	8	18.02 ± 0.28	1.7 ± 1.1	0.32	1.3
κ^1 Cet	20630	178.2	-43.1	9.14	20.84	12.68 ± 0.13	DI	8	17.49 ± 0.13	0.50 ± 0.15	1.36	-5.8
EP Eri	17925	192.1	-58.3	10.4	19.50	13.13 ± 0.10	DI	11	17.94 ± 0.10	1.40 ± 0.32	1.00	1.3
β Gem	62509	192.2	23.4	10.4	19.65	13.20 ± 0.10	DI	3	18.01 ± 0.10	1.65 ± 0.38	1.08	1.5
13 Per	16895	141.2	-9.6	11.1	16.45	12.61 ± 0.02	FeII	8	18.28 ± 0.11	3.09 ± 0.81	3.00	0.1
γ Ser	142860	27.7	45.7	11.3	-18.19	12.33 ± 0.10	FeII	8	18.00 ± 0.15	1.62 ± 0.56	0.13	2.7
HR 1925	37394	158.4	11.9	12.3	17.50	13.43 ± 0.005	DI	6	18.239 ± 0.012	2.81 ± 0.56	2.45	0.6
α Aur	34029	162.6	4.6	13.1	21.48	13.44 ± 0.02	DI	4	18.247 ± 0.023	2.86 ± 0.15	2.50	2.4
HR 8	166	111.3	-32.8	13.7	6.50	13.466 ± 0.006	DI	6	18.273 ± 0.013	3.04 ± 0.61	2.51	0.9
72 Her	157214	55.9	32.3	14.3	-15.51	14.32 ± 0.44	FeII	8	19.99 ± 0.45	$160 \pm 170^{\text{b,c}}$	0.36	...
π^1 UMa	72905	150.6	35.7	14.4	12.49	13.33 ± 0.02	DI	12	18.137 ± 0.023	2.22 ± 0.12	1.96	2.2
V1119 Tau	35296	187.2	-10.3	14.4	23.47	12.80 ± 0.14	DI	13	17.61 ± 0.14	0.66 ± 0.21	1.38	-3.4
99 Her	165908	57.0	22.3	15.6	-17.43	13.27 ± 0.14	FeII	8	18.94 ± 0.18	$14.1 \pm 5.8^{\text{b}}$	0.43	...
σ Boo	128167	45.6	67.2	15.8	-2.58	11.82 ± 0.14	FeII	14	17.49 ± 0.18	0.50 ± 0.21	0.18	1.5
σ Boo	128167	45.6	67.2	15.8	-2.28	11.23 ± 0.10	MgII	14	16.67 ± 0.27	$0.076 \pm 0.047^{\text{d}}$	0.18	...
β Cas	432	117.5	-3.3	16.8	9.15	13.38 ± 0.08	DI	3,15	18.187 ± 0.081	2.49 ± 0.46	2.42	0.2
τ^6 Eri	23754	217.4	-50.3	17.6	16.99	12.71 ± 0.12	FeII	14	18.38 ± 0.16	3.9 ± 1.5	0.56	2.2
τ^6 Eri	23754	217.4	-50.3	17.6	16.99	13.01 ± 0.08	MgII	14	18.45 ± 0.26	$4.6 \pm 2.7^{\text{d}}$	0.56	...
DX Leo	82443	201.2	46.1	17.8	11.00	12.88 ± 0.15	DI	11	17.69 ± 0.15	0.79 ± 0.28	0.44	1.3
V368 Cep	220140	118.5	16.9	19.2	6.00	13.13 ± 0.10	DI	11	17.94 ± 0.05	1.40 ± 0.32	1.81	-1.3
α Tri	11443	138.6	-31.4	19.4	17.89	13.30 ± 0.10	DI	3	18.11 ± 0.10	2.07 ± 0.48	3.12	-2.2
HR 4345	97334	184.3	67.3	21.9	4.30	13.00 ± 0.01	DI	6	17.807 ± 0.015	1.04 ± 0.21	0.35	3.3
SAO 136111	73350	232.1	20.0	24.0	12.00	13.339 ± 0.009	DI	6	18.146 ± 0.014	2.27 ± 0.45	0.15	4.7
λ And	222107	109.9	-14.5	26.4	6.50	13.68 ± 0.15	DI	5	18.49 ± 0.15	4.97 ± 1.72	2.07	1.7
λ And	222107	109.9	-14.5	26.4	4.52	12.92 ± 0.26	FeII	16	18.59 ± 0.28	6.3 ± 4.1	2.32	1.0
λ And	222107	109.9	-14.5	26.4	4.97	13.17 ± 0.22	MgII	16	18.61 ± 0.33	$6.6 \pm 5.0^{\text{d}}$	2.32	...
σ Cet	15798	191.1	-63.8	26.7	15.99	13.19 ± 0.10	FeII	8	18.86 ± 0.15	$11.7 \pm 4.1^{\text{b}}$...
HR 860	17948	137.2	2.2	26.7	15.10	12.60 ± 0.03	FeII	8	18.27 ± 0.12	3.02 ± 0.80	2.76	0.3
SAO 32862	198084	94.4	9.1	27.3	-2.60	12.80 ± 0.02	FeII	8	18.47 ± 0.11	4.8 ± 1.3	1.28	2.8

Table 2 continued on next page

Table 2 (*continued*)

Star	HD	l	b	d	v	$\log N(\text{Ion})$	Ion	Reference	$\log N(\text{H I})$	$d_{\text{obs}}^{\text{edge}}$	$d_{\text{model}}^{\text{edge}}$	σ^a
Name	#	(deg)	(deg)	(pc)	(km s ⁻¹)	(cm ⁻²)			(cm ⁻²)	(pc)	(pc)	
η Ari	13555	147.1	-37.8	28.9	16.99	12.38 ± 0.05	FeII	8	18.05 ± 0.12	1.82 ± 0.51	3.03	-2.4
PW And	1405	114.6	-31.4	29.0 ^e	8.50	13.23 ± 0.10	DI	11	18.04 ± 0.10	1.76 ± 0.41	2.64	-2.1
SAO 85045	157466	47.5	29.8	29.3	-19.02	13.70 ± 0.36	FeII	8	19.37 ± 0.38	38 ± 33^b	0.27	...
SAO 85045	157466	47.5	29.8	29.3	-19.02	14.15 ± 0.59	MgII	8	19.59 ± 0.64	$63 \pm 93^{b,c,d}$	0.27	...
δ Cas	8538	127.2	-2.4	30.5	13.05	12.795 ± 0.1	MgII	10,17	18.24 ± 0.27	2.8 ± 1.7	2.69	0.1
HR 1099	22468	184.9	-41.6	30.7	21.90	13.06 ± 0.03	DI	15	17.867 ± 0.032	1.193 ± 0.088	1.16	0.4
α Gru	209952	350.0	-52.5	31.0	-10.93	12.98 ± 0.11	FeII	14	18.65 ± 0.16	7.2 ± 2.6	0.18	2.7
α Gru	209952	350.0	-52.5	31.0	-10.93	13.79 ± 0.22	MgII	14	19.23 ± 0.33	$28 \pm 21^{b,d}$	0.18	...
DK UMa	82210	142.6	38.9	31.9	9.41	13.14 ± 0.01	DI	8	17.947 ± 0.015	1.434 ± 0.049	1.78	-7.0
ϵ Gru	215789	338.3	-56.5	39.5	-7.30	12.86 ± 0.1	FeII	18	18.53 ± 0.15	5.5 ± 1.9	0.18	2.8
ϵ Gru	215789	338.3	-56.5	39.5	-7.30	13.95 ± 0.1	MgII	18	19.39 ± 0.27	$40 \pm 24^{b,d}$	0.18	...
101 Tau	31845	185.1	-16.0	40.8	22.40	12.49 ± 0.05	MgII	19	17.93 ± 0.25	1.38 ± 0.80	1.46	-0.1
SAO 93981	28568	180.5	-21.4	41.5	23.90	13.21 ± 0.02	DI	6	18.017 ± 0.023	1.685 ± 0.089	1.72	-0.4
SAO 111879	28736	190.2	-27.6	43.5	21.60	12.65 ± 0.05	MgII	19	18.09 ± 0.25	2.0 ± 1.2	1.08	0.8
V471 Tau	...	172.5	-27.9	44.1	20.90	13.382 ± 0.007	DI	6	18.189 ± 0.013	2.50 ± 0.50	2.20	0.6
SAO 76593	27808	174.8	-19.1	44.3	23.10	12.86 ± 0.11	MgII	19	18.30 ± 0.27	3.2 ± 2.0	2.14	0.5
SAO 76683	29419	176.0	-15.6	44.5	23.20	12.69 ± 0.08	MgII	19	18.13 ± 0.26	2.2 ± 1.3	2.09	0.1
SAO 93982	28608	185.1	-24.7	44.7	23.20	12.42 ± 0.06	MgII	19	17.86 ± 0.25	1.17 ± 0.69	1.33	-0.2
SAO 93831	26784	182.4	-27.9	45.0	23.00	12.32 ± 0.13	MgII	19	17.76 ± 0.28	0.93 ± 0.60	1.45	-0.9
SAO 94033	29225	181.6	-20.5	45.7	22.50	12.68 ± 0.04	MgII	19	18.12 ± 0.25	2.1 ± 1.2	1.65	0.4
SAO 93963	28406	178.8	-20.6	46.4	22.10	12.67 ± 0.07	MgII	19	18.11 ± 0.26	2.1 ± 1.2	1.86	0.2
SAO 93945	28237	183.7	-24.7	46.4	22.40	12.42 ± 0.12	MgII	19	17.86 ± 0.27	1.17 ± 0.74	1.42	-0.3
V993 Tau	28205	180.4	-22.4	47.0	23.30	13.18 ± 0.01	DI	6	17.987 ± 0.015	1.572 ± 0.054	1.72	-2.7
SAO 76609	28033	175.4	-18.9	49.4	23.60	13.33 ± 0.02	DI	6	18.137 ± 0.023	2.22 ± 0.12	2.11	0.9
SAO 56530	21847	156.2	-16.6	49.5	21.10	13.14 ± 0.37	MgII	19	18.58 ± 0.44	6.2 ± 6.3^c	2.90	...
SAO 93885	27561	180.4	-24.3	52.4	22.20	12.50 ± 0.06	MgII	19	17.94 ± 0.25	1.41 ± 0.83	1.68	-0.3
SAO 93913	27848	178.6	-22.0	53.5	22.40	12.56 ± 0.24	MgII	19	18.00 ± 0.34	1.6 ± 1.3	1.86	-0.2
HR 1608	32008	209.6	-29.4	54.0	21.60	13.02 ± 0.05	DI	6	17.827 ± 0.051	1.09 ± 0.22	0.59	2.3
45 Aur	43905	161.1	17.3	59.2	18.47	12.47 ± 0.03	FeII	8	18.14 ± 0.12	2.24 ± 0.60	2.29	-0.1
G191-B2B	...	156.0	7.1	59.9	19.19	13.36 ± 0.03	DI	8	18.167 ± 0.032	2.38 ± 0.18	2.59	-1.2
ι Cap	203387	33.6	-40.8	60.3	-12.06	13.11 ± 0.33	DI	8	17.92 ± 0.33	1.3 ± 1.0	0.50	0.8
η Aur	32630	165.4	0.3	74.6	21.5	12.27 ± 0.08	FeII	20	17.94 ± 0.14	1.41 ± 0.45	2.48	-2.4
Feige 24	...	166.0	-50.3	91.7	17.60	13.19 ± 0.14	DI	21	18.00 ± 0.14	1.61 ± 0.52	1.67	-0.1

^a $(d_{\text{obs}}^{\text{edge}} - d_{\text{model}}^{\text{edge}})/\sigma(d_{\text{obs}}^{\text{edge}})$ ^b Sight line ignored because observed value is $>5\sigma$ from median value.^c Sight line ignored because relative error $(\sigma(d_{\text{obs}}^{\text{edge}})/d_{\text{obs}}^{\text{edge}})$ is of order unity (i.e., >0.9).^d This measurement is not used in the subsequent analysis. Preference is given instead to the complementary Fe II measurement.^e Metchev & Hillenbrand (2009)

References—(1) Bertin et al. (1995); (2) Hébrard et al. (1999); (3) Dring et al. (1997); (4) Linsky et al. (1995); (5) Wood et al. (1996); (6) Wood et al. (2005); (7) Wood & Linsky (1998); (8) Redfield & Linsky (2004a); (9) Lallement et al. (1995); (10) Ferlet et al. (1995); (11) Wood et al. (2000); (12) Wood et al. (2014b); (13) Wood et al. (2014a); (14) Redfield & Linsky (2002); (15) Piskunov et al. (1997); (16) Malamut et al. (2014); (17) Lallement & Ferlet (1997); (18) Lecavelier des Etangs et al. (1997); (19) Redfield & Linsky (2001); (20) Welsh & Lallement (2010); (21) Vennes et al. (2000).

Table 3. LIC Model Parameters

Property	Parameter
Sight lines used	62
x_{center} (pc)	−0.8 pc
y_{center} (pc)	+0.7 pc
z_{center} (pc)	−0.4 pc
reduced χ^2	8.3
Median difference (pc)	0.40
Spherical Harmonic coefficients	
$a_{0,0}$	+4.708
$a_{1,0}$	−0.519
$a_{1,-1}$	+0.421
$a_{1,+1}$	−0.524
$a_{2,0}$	+0.197
$a_{2,-1}$	−0.360
$a_{2,+1}$	+0.172
$a_{2,-2}$	−0.193
$a_{2,+2}$	+0.022

Table 4. Composition of Gas Along Selected Lines of Sight

Star	l	b	$d(\text{pc})$	Cloud ^c	$\log[N(\text{H I})]^c$	$\Delta d(\text{neutral})^d$	$\Delta d(\text{ionized})^d$
α Cen ^a	315.7	-0.9	1.32	G	17.6	0.70	0.62
Sirius A	227.2	-8.9	2.64	LIC	17.2	0.25	
				Blue	17.2	0.25	
				Sum		0.50	2.14
ϵ Eri ^a	5.8	-48.1	3.22	LIC	17.8	1.10	2.12
61 Cyg ^a	82.3	-5.8	3.49	Aql	17.8	1.10	
				Eri	17.8	1.10	
				Sum		2.20	1.29
Procyon	213.7	+13.0	3.51	LIC	17.9	1.56	
				Aur	17.6	0.70	
				Sum		2.26	1.25
ϵ Ind ^a	336.2	-48.0	3.63	LIC	16.6	0.14	3.49
61 Vir ^a	311.9	+44.1	8.53	NGP	(18.0)	(1.7)	(6.8)
β Com	43.5	+85.4	9.15	NGP	(18.0)	(1.7)	(7.4)
π^1 UMa	150.6	+35.7	14.6	LIC	17.85	2.30	12.3
τ Boo	358.9	+73.9	15.6	NGP	(18.0)	(1.7)	13.9
51 Peg	90.1	-34.7	15.6	Eri	(17.9)	(1.6)	
				Hya	(17.4)	(0.4)	
				Sum		(2.0)	(13.6)
χ Her ^b	67.7	+50.3	15.9	NGP	(18.0)	(1.7)	14.2

^a Astrosphere detected by [Wood et al. \(2005\)](#) indicates that a cloud with neutral hydrogen must surround the star.

^bNo astrosphere detected by [Wood et al. \(2005\)](#).

^c Cloud identification and hydrogen column densities from [Redfield & Linsky \(2008\)](#).

^d Distance (pc) to the star through neutral and ionized gas.

Table 5. Are clouds in and near the hydrogen hole Strömgren shells?

Line of sight through	$\log N(\text{H I})$	cloud	thickness (pc)	property
Strömgren shell	17.10		0.2	for $n(\text{H I})=0.2 \text{ cm}^{-3}$
ϵ CMa	16.76	Blue	0.12	shell (1/e EUV photons absorbed)
ϵ CMa	17.34	LIC	0.35	most EUV photons absorbed
Sirius	17.2	Blue	0.25	shell (1/e photons absorbed)
Sirius	17.2	LIC	0.25	shell (1/e photons absorbed)
ζ Dor	17.8	Blue	1.0	all EUV photons absorbed
HR 2225	17.9	Blue	1.3	all EUV photons absorbed

Table 6. Stars located Inside and Near the Hydrogen Hole

Star	HD	d (pc)	l	b	Solar H wall	LIC detection	Other clouds	Hydrogen hole
ζ Dor	33262	11.7	226	-36	N	N	Blue, Dor	inside
HR 2225	43162	16.7	230	-18	N	N	Blue	inside
β Pic	39060	19.3	258	-31	—	N	Blue	inside
HR 2882	59967	21.8	250	-9	N	N	Blue	inside
β Car	80007	34.1	286	-14	—	N	Blue, G	inside
HR 2265	43940	61.9	245	-22	—	N	Blue, Dor	inside
WD 0621-376	—	78	245	-21	—	N	Blue, Dor	inside
α Car	45348	96	261	-25	—	N	Blue	inside
ϵ CMa	52089	124	239.8	-11.4	—	Y	Blue, other	inside
Sirius	48915	2.6	227	-9	Y	Y	Blue	edge
EP Eri	17925	10.4	192	-58	—	Y	Blue	edge
SAO 136111	73350	23.6	232	+20	N	Y	—	edge
σ Cet	15798	25.8	191	-64	—	Y	Blue, G	edge
β CMa	44743	151	226.1	-14.3	—	N	Blue, other	edge
α Cen	128620	1.3	315	-1	Y	N	G	outside
70 Oph A	165341	5.1	30	+11	Y	N	G, Aql, Oph	outside
36 Oph	155886	6.0	358	+7	Y	N	G	outside
δ Pav	190248	6.1	329	-32	Y	N	Vel, Dor	outside
HR 6748	165185	17.4	356	-7	Y	N	Aql	outside
ρ Oct	137333	66	307	-23	—	N	Blue, G	outside